Elsevier Editorial System(tm) for Surface and Coatings Technology

Manuscript Draft

Manuscript Number: SURFCOAT-D-20-02420R2

Title: Graphene-coated Ti-Nb-Ta-Mn foams: A promising approach towards a suitable biomaterial for bone replacement

Article Type: Full Length Article

Keywords: Biomaterials; Titanium alloys; Powder Metallurgy; - Nanocoatings; Graphene; Cytotoxicity

Corresponding Author: Dr. sheila Katherine Lascano, Dr. Eng.

Corresponding Author's Institution: Universidad Técnica Federico Santa María

First Author: sheila Katherine Lascano, Dr. Eng.

Order of Authors: sheila Katherine Lascano, Dr. Eng.; Ricardo Chávez Vásconez, Eng.; Daniela Muñoz Rojas, Eng.; Juliet Aristizabal, PhD.; Barbara Arce, BS. Phys.; Carolina Parra, PhD.; Cristian Acevedo, Dr.; Nicole Orellana, BS.Biochem; Mauricio Reyes Valenzuela, Eng.; Francisco Gotor, Dr.; Cristina Arévalo, Dr. Eng.; Yadir Torres Hernández, PhD.

Abstract: The design of bone implants with proper biological and mechanical properties remains a challenge in medical implantology. The use of bioactive coatings has been shown to improve the biocompatibility of the implant surface. In this study, a new approach including porous scaffolds, β-Ti alloys and nanocoatings to design new bone implants is presented. Porous Ti-Nb-Ta-xMn alloys (x: 2, 4, and 6 wt.%) substrates were obtained by powder metallurgy and the effect of the porosity and Mn content on mechanical properties was studied. CVD single-layer graphene was transferred onto the porous substrates that presented the best mechanical response (x: 4 wt.%) for further evaluation of in vitro cell behavior (biocompatibility and cell adhesion). Cytotoxicity and biocompatibility tests confirmed that cell adhesion and proliferation were successfully achieved on graphene-coated porous substrates, confirming these systems are potential candidates for using in partial bone tissue replacement.

Graphene-coated Ti-Nb-Ta-Mn foams: A promising approach towards a suitable biomaterial for bone replacement

*Sheila Lascano[1,] *, Ricardo Chávez-Vásconez[1], Daniela Muñoz-Rojas[1], Juliet Aristizabal[2], Bárbara Arce[2], Carolina Parra[2], Cristian Acevedo[2], Nicole Orellana[3], Mauricio Reyes-Valenzuela[1], Francisco José Gotor[4], Cristina Arévalo[5], Yadir Torres[5]*

[1] Departamento de Ingeniería Mecánica, Universidad Técnica Federico Santa María, Avda. Vicuña Mackenna N° 3939- San Joaquín, Santiago, Chile.

[2] Departamento de Física, Universidad Técnica Federico Santa María, Av. España 1680, Valparaíso, Chile

[3] Centro de Biotecnología "Dr. Daniel Alkalay Lowitt". CB-DAL, Universidad Técnica Federico Santa María, Av. España 1680, Valparaíso, Chile.

[4] Instituto de Ciencia de Materiales de Sevilla (CSIC-US), Américo Vespucio 49. 41092 Sevilla, Spain.

[5] Departamento de Ingeniería y Ciencia de los Materiales y del Transporte, Escuela Politécnica Superior, Calle Virgen de África 7, 41011 Seville, Spain.

Keywords: biomaterials; titanium alloys; powder metallurgy; nanocoatings; graphene; cell adhesion, cytotoxicity.

Abstract

The design of bone implants with proper biological and mechanical properties remains a challenge in medical implantology. The use of bioactive coatings has been shown to improve the biocompatibility of the implant surface. In this study, a new approach including porous scaffolds, β-Ti alloys and nanocoatings to design new bone implants is presented. Porous Ti-Nb-Ta-xMn alloys (x: 2, 4, and 6 wt.%) substrates were obtained by powder metallurgy and the effect of the porosity and Mn content on mechanical properties was studied. CVD single-layer graphene was transferred onto the porous substrates that presented the best mechanical response (x: 4 wt.%) for further evaluation of in vitro cell behavior (biocompatibility and cell adhesion). Cytotoxicity and biocompatibility tests confirmed that cell adhesion and proliferation were successfully achieved on graphene-coated porous substrates, confirming these systems are potential candidates for using in partial bone tissue replacement.

1. Introduction

Metallic biomaterials are extensively used for replacing hard tissue and for load-bearing applications. Specifically, titanium and its alloys exhibit the most suitable characteristics for biomedical applications, promoting *in vitro* and *in vivo* behavior [1]. However, these materials have shown important drawbacks that compromise the reliability of implants: stress-shielding phenomenon, poor or low osseointegration, and fracture of implants due to overload or accumulated damage produced by fatigue.

The first drawback, the stress-shielding phenomenon [2], is caused by the mismatch between Young's modulus of bone tissue and titanium implant (20-25 GPa for cortical bone and 110 GPa for cp- Ti and α+β type Ti) [3], and promotes bone resorption and eventual fracture of the host tissue [4], compromising the clinical success of implants [5]. An approach to solve this issue is the design and manufacture of porous metallic biomaterials that combine the low stiffness of porous structures [6-8] and the high strength of metallic alloys [9].

The control of microstructural parameters of porous materials such as porosity content, pore size distribution, pore morphology, and interconnectivity has become an attractive strategy to reduce stress shielding as well as to promote bone in-growth [10]. Different fabrication methods are currently employed for the manufacture of metallic foams [9, 11-16]. Among these methods, powder metallurgy (PM) is a promising route since offers cost-effective and flexible fabrication of tailored titanium foams for biomedical applications[17] and allows the design and manufacture of new alloys that cannot be produced by casting approaches. The use of the space-holder technique arises as a suitable and economic route for introducing high levels of porosity (35-80%) and a homogeneous pore distribution throughout the Ti volume [8, 18, 19]. Different materials can be employed as temporary space-holder particles which are later eliminated by two alternative methods: evaporation at low temperatures, in the case of ammonium bicarbonate [20-

22], carbamide [15, 17, 23], K_2CO_3 [24], polymethyl methacrylate (PMMA) [25, 26] and poly-vinyl alcohol (PVA) [27], or dissolution in water, in the case of sodium chloride [6, 21, 28, 29]. It is also important to highlight that, the higher the porosity, the lower the mechanical strength and wear resistance of the porous structure. One approach to address this specific issue in titanium alloys is to reduce the stiffness by designing alloys with low Young's modulus.

Two generations of Ti alloys have been developed for biomedical applications [30, 31]. The first generation of titanium alloys, which exhibit both α and (α+β) phases, was developed between 1950 and 1990 and extensively used for implants. However, these alloys showed some drawbacks, specifically poor wear resistance, low hardness, and high Young's modulus (~110 GPa) [32, 33]. In addition, depending on the elements present in these alloys, a cytotoxic effect has to be taken into account [34-36]. Ti, Zr, Ta and Pd are low cytotoxicity elements [32], whereas other elements such as Al, V, Ni, and Co have been reported as cytotoxic [34, 37, 38]. Aluminum, for instance, has been found to increase scar tissue and is involved in severe neurological and metabolic-bone diseases, such as Alzheimer's and osteomalacia [39]. Vanadium produces a severe tissue reaction that is characterized by a sterile abscess [32] whereas nickel exhibits one of the highest sensitivities in metallic allergen tests [40], producing contact allergenic reactions and carcinogen effects [41].

In response to these drawbacks**,** a second generation of Ti alloys, the β-phase Ti-based alloys, have been developed and used since the 1990s. These alloys have been preferred for bio-implant applications rather than α or (α+β) Ti alloys, mainly due to their lower elastic modulus [42]. In these β-type Ti alloys, the presence of β-phase is promoted by incorporating β-stabilizing elements, such as Pd, Ni, Mo, Ta, V, Mn, and Nb [43]. Biesiekierski, et al. [34] have identified the biological impact of some of those elements on human health, assessing their biocompatibility and other potential risks such as corrosion, degradation, and their carcinogenic,

genotoxic, mutagenic, cytotoxic and allergenic properties. According to literature, Ti, Nb, Ta, Mn, Zr, and Ru, have been found to exhibit the best biofunctional behavior [42]. Among those elements, Ta, Nb, and Zr have been reported to impact the mechanical properties of β titanium alloys, by decreasing their elastic modulus while increasing their strength [44, 45]. Some reports illustrating this behavior of Ti-30Nb-13Ta, Ti-13Nb-13Zr, and Ti-35Nb-7Zr-5Ta can be found in Ref [46-49]. These alloys have been developed with the aim to match Young's moduli of different types of human bone (cortical: 3–30 GPa; cancellous: 0.02–0.5 GPa). One route to decrease Young's modulus of a Ti-based alloy is by increasing its bond order (B_o) and energy level (M_d) [34,50]. For bone replacement applications, the target bond order value is 2.92 eV, and whereas the target energy level is 2.38 eV. The B_o and M_d values can be obtained using the equations (1) and (2) [50], where X_i is the atomic fraction of each alloying element:

$$\overline{B_o} = \sum_i X_i (B_o)_i \qquad (1)$$

$$\overline{M_d} = \sum_i X_i (M_d)_i \qquad (2)$$

Efforts are now focused on finding new alloying elements to improve the mechanical and corrosion properties of metallic biomaterials. In particular, Mn is an interesting alternative due to its role in cartilage and collagen formation, bone mineralization [51], and cell adhesion [52]. However, only a few studies have reported the effect of Mn on Ti alloys properties, especially in the second-generation alloys [53]. Good corrosion behavior of Mn-containing alloys in simulated body fluid has been recently reported [54].

In author's previous work, Ti-34Nb-29Ta-xMn (x: 2, 4, and 6 wt.%) alloy foams fabricated by mechanical alloying were studied, showing elastic moduli ranging between 27 and 30 GPa [55]. These results, in the range of cortical bone, suggested that this specific Ti alloy is not expected to exhibit a strong stress-shielding effect. Although these results are promising, the overall cost of material fabrication, related to long processing time (~60 hours), is a relevant aspect that still needs to be addressed.

Another important disadvantage of Ti-based materials is their poor or low rate of osseointegration caused by the formation of fibrous tissue at the bone-implant interface, which promotes micro-movements of the implant and eventual loosening, whether this is of aseptic nature or caused by the presence of bacterial biofilms. The use of thermochemical treatments and/or bioactive coatings has been proposed to modify the surface texture to improve the bioactivity of Ti implants. Some techniques to enhance the cell adhesion to implant surface include anodic reaction, hydrogen peroxide, sol-gel, thermochemical surface modification, and chemical vapor deposition. [56]. Although rough and porous surfaces have proven to increase fixation of Ti implants [57, 58], to obtain reliable implants it is essential to generate bioactive surfaces that promote cell adhesion and ingrowth, preventing bacteria proliferation. In this sense, bioactive coatings, such as hydroxyapatite and bioactive glass, have shown positive results in terms of osseointegration.

In this context, surface modification at the nanometric scale represents a unique framework to improve the biofunctionality of porous materials [59]. Nanostructured coatings have been designed and applied to non-porous titanium surfaces to control cell behavior and to obtain bioactive surfaces, promoting cell adhesion and proliferation [60, 61]. Graphene-family nanomaterials have been widely used in the biomedical field because of their various unique properties. Graphene supports the absorption and binding of antibodies, adapters, drugs, genes, enzymes, and other molecules [62], has been explored for cancer treatments [63], has been used for biological imaging [64], as drug carrier [65], biosensor [66], and biological scaffold in tissue engineering [67]. Previous studies have revealed that scaffolds based on graphene and its derivatives, such as graphene oxide, can enhance cell differentiation [68-70]. It has been also proven that single-layer graphene (SLG) promotes the osteogenic differentiation into osteogenic lineages when used as a coating onto titanium samples. This nanomaterial, that can be grown as large as 50cm x 5cm [71], improves the initial fixation strength and long-term osseointegration of

the implant/bone interface required for further promotion of bone defect healing in Ti6Al4V [72]. However, Al and V are considered as hazardous elements that could compromise long term implantation in the human body [32, 73], as was mentioned before.

The aim of this work is to propose a novel approach based on the use of graphene-coated porous Ti-Nb-Ta-Mn alloys produced by space-holder technique, aim to present low Young's modulus for stress-shielding reduction and to increase osseointegration and cell viability and proliferation. For the selection of the optimal chemical composition of Ti alloys, theoretical calculus was used to estimate the atomic fraction of each element as well as the data obtained in previous works, where an α + β Ti phase was processed via mechanical alloying and conventional sintering [54, 55]. Using this background, which will be discussed in detail in the following sections, a specific Ti alloy foams composition was selected, Ti-35Nb-29Ta-xMn (x: 2, 4, 6 wt.%), for implant applications. In this work the effect of physical and processing parameters of Ti alloys, such as Mn content, sintering temperature, and porosity, on its microstructural characteristics and mechanical properties, was investigated and compared with the reported values for porous commercially pure titanium (c.p. Ti) grade 4 samples [21]. This porous material, fabricated by space-holder technique, was coated with high-quality single-layer graphene to promote a bioactive surface and increase the material's biofunctionality and further osseointegration. Biocompatibility and biological behavior of coated and uncoated substrates were evaluated by in vitro cytotoxicity tests using Mouse Embryonic Fibroblasts (MEF).

2. Materials and methods

The percentage of each alloying element in Ti-35Nb-29Ta-xMn (x: 2, 4, 6 wt.%) alloys was selected following two main criteria: (i) to look for an adequate concentration of β stabilizing elements required to retain the β phase at room temperature, and (ii) to tune the bond order and

energy level needed to achieve a Young's modulus close to the modulus of the bone (~ 30 GPa) to minimize the stress shielding.

Regarding the first criterium, the equation (3), (based on Ref [74]) allows obtaining the equivalent Nb fraction (Nb_{eq}), as a function of Mn and Ta content, to achieve the stabilized β phase in the alloy.

$$Nb_{eq} = Nb + \frac{at.\%\ Nb}{at.\%\ Ta}Ta + \frac{at.\%\ Nb}{at.\%\ Mn}Mn \quad (3)$$

Using the reported atomic percent (at. %) values to obtain a stable β phase (21 at. % for Ta, 5.3 at. % for Mn and 23 at. % for Nb) [74], the calculated Nb_{eq} for the Ti-35Nb-29Ta-xMn alloy was 54.5 at. % (for 2 wt.% Mn), 67.7 at. % (for 4 wt.% Mn) and 80.4 at. % (for 6 wt.% Mn).

Concerning the second criterium, the B_o and M_d values for the Ti-35Nb-29Ta-xMn alloy can be obtained using the equations (1) and (2) [50]. The optimum B_o and M_d calculated values are 2.925 eV and 2.376 eV, respectively. These values place the selected alloy in the region where Young's modulus will be theoretically between 50-60 GPa.

2.1. Fabrication and characterization of the porous substrates

Ti-35Nb-29Ta-xMn (x: 2, 4 and 6 wt.%) and c.p. Ti grade 4 (reference material) porous samples were fabricated using space-holder technique. For sample processing, metallic powders and NH_4HCO_3 (50 vol.%) particles were blended for 40 min in a vacuum chamber (Plas-Lab) to reach good homogenization. Morphological characterization and information of commercial powders prior to this blending procedure are shown in Figure S1 and Table S1. The particle size distribution for spacer material was determined by sieve analysis. Then, uniaxial cold compaction of powders was performed using a universal testing machine Zwick Roell at 400 MPa (according to compressibility curves of mixed powders). A preload of 20 MPa was applied at a rate of 8

mm/min followed by a compaction loading rate of 6 kN/s, using 3 min dwell time and 15 min unloading time. The dimension of specimens (height/diameter = 2 and 13 mm die diameter) was chosen to suit compression test requirements, according to ASTM E9 [75] and ISO 13314 [76]. Subsequently, NH_4HCO_3 from green samples was thermally eliminated by heating the samples at 60 °C for 13 hours followed by a second treatment at 100 °C for 10 hours [21]. Finally, the porous substrates were sintered at different temperatures, 1250 °C (c.p. Ti), 1200 °C and 1300 °C (Ti alloys), for 2 h under high vacuum conditions (~10^{-5} mbar) in a CARBOLYTE STF 15/75/450 ceramic furnace with a horizontal tube. These temperatures were chosen to favor the largest amount of β-Ti phase [77] and to guarantee the quality of the sintering necks.

After sintering, the physical, microstructural, and mechanical properties of these samples were studied. The density, total porosity (P(Arch)) and interconnected porosity (Pi) of the metallic foams were determined by the Archimedes' method, using distilled water as immersion liquid, to evaluate the influence of processing parameters and composition on their physical features. P(Arch) and Pi were calculated from the density measurements, according to the ASTM C373 standard [78], chosen for its reliability and simplicity. Then, the porous substrates were prepared for microstructural analysis, by conventional metallographic steps consisting of mounting them into a resin, grinding, polishing, and mechano-chemical polishing using colloidal silica and hydrogen peroxide. Size, morphology, and roughness of substrate pores were investigated through optical microscopy (OM), image analysis (IA) (Nikon Epiphot optical microscope), and scanning electron microscopy (SEM) (Carl Zeiss model EVO MA 10). In particular, OM together with Image-Pro Plus software were used to evaluate the morphological parameters of pores. The following pore parameters were characterized: (i) the total porosity, via image analysis (P(IA)); (ii) the equivalent pore diameter (Deq), defined as the average diameter measured from the pore centroid; (iii) the pore shape factor ($Ff = 4\pi A/(PE)^2$), where A is the pore area and PE is the experimental perimeter of the pore; and (iv) the mean size of the neck between the pores (λ).

Results were expressed as mean value ± standard deviation, except for Deq where the results were reported as mean value ± error because the variability of results. Analysis of variance (ANOVA) was carried out for pore shape factor and equivalent pore diameter data, followed by a Tukey's post-test using Statgraphics software. Significance was considered for p values of $p < 0.05$. X-ray diffraction (XRD) analysis was performed on the porous substrates using a PANalytical X'Pert Pro instrument equipped with a θ/θ goniometer, using Cu Kα radiation (40 kV, 40 mA) and a secondary Kβ filter and the X'Celerator detector. The diffraction patterns were scanned from 20º to 120º (2θ) in the step-scan mode using a step size of 0.017º and a counting time of 400 s/step. A long counting time was chosen to detect the existence of any possible secondary phase in the sintered samples. The XRD data was plotted using a log y-scale to easily identify these minor phases. The crystallographic structure of Ti alloy samples was studied by transmission electron microscopy, (S)TEM, using a FEI Talos F200S microscope operated at an accelerating voltage of 200 kV. The lamella preparation was carried out using a dual-beam focused ion beam (FIB)-SEM system (Carl Zeiss Auriga). Ga ion beam source at 30 kV and different currents, decreasing from 600 pA to 50 pA, was used for milling the sample until reaching electron transparency.

Finally, the mechanical behavior of the samples was characterized by compression tests, using a universal electromechanical Zwick Roell machine Z100 and applying a 0.005 mm/mm/min strain rate up to a strain of ≈ 25%, according ASTM E9 [75] and ISO 13314: 2011 [76]. The yield strength (σ_y) values were obtained from the stress-strain curves, based on the method proposed by R. M. Christensen [79]. The obtained Young's modulus (E_c) was compared with those calculated using the model proposed by Nielsen ($E_{Nielsen}$) [80]. The samples with the Young's modulus closest to human bone and best yield strength were selected for the following coating process using graphene.

2.2. Deposition and characterization of graphene coatings

Single Layer Graphene (SLG) was selected as a coating due to its potential to produce a bioactive surface that promotes initial adhesion, cultivation and cell growth, and its ability to suppress bacteria growth [81, 82]. SLG was grown by chemical vapor deposition (CVD) onto a 25 μm thick copper foil (purity >99.8%, Alfa Aesar). The growth process was carried out using CH_4 and H_2 as precursor gases (20 sccm and 10 sccm, respectively). The growth temperature was set at 1050 °C for 2 hours and the pressure was kept at 0.18 mtorr using a Pfeiffer Vacuum Hi-Cube pump station. After the graphene growth step, the copper sample was naturally cooled down in the Ar atmosphere. SLG was transferred onto the porous substrates using a variation of the Polymethyl methacrylate (PMMA)-assisted method [82-84]. This six-step process is summarized in Figure 1. A thin layer of PMMA (350,000 Mw dissolved in toluene at 7% w/v) was spin-coated onto the graphene grown on copper (step 1). After that, the backside of the coated sample was wetly etched using a 10% HNO_3 solution for 1 minute (step 2). This procedure helps to remove the graphene layer grown at the back of the Cu foil. The final detachment of the PMMA/graphene layer from the copper foil was carried out by chemical etching using 0.1 M ammonium persulfate (APS) aqueous solution (step 3). PMMA/graphene layer was rinsed with deionized water (step 4) and then manually transferred onto the porous substrate using a one-step procedure, which involves the transfer onto the substrate and the subsequent removal of the PMMA film using 2-Propanol (step 5). Finally, the coated porous sample was baked at 120 °C for 5 minutes to improve the adhesion of graphene coating to the substrate (step 6).

Graphitic quality and atomically resolved imaging of CVD graphene grown on Cu were characterized by Raman spectroscopy (inVia, Renishaw, 532 nm laser) and Scanning Tunneling Microscopy (VT-STM Omicron), respectively. Graphene was transferred onto a SiO_2 sample,

using the same PMMA-assisted method, to obtain a clean Raman signature without the strong fluorescence contribution of Cu substrate. Morphology of graphene transferred onto Ti-35Nb-29Ta-4Mn foams was examined using OM (Nikon Eclipse LV100ND) and Variable Pressure SEM [85] (Quanta FEG-250 SEM). Raman spectroscopy was used to confirm the presence of the SLG coating onto the porous substrate and to evaluate the quality of the transference process.

2.3. Cytotoxicity and biocompatibility test

The biocompatibility of uncoated and graphene-coated porous substrates was studied using MEF (ATCC cell line, USA). MEF can be considered pre-osteoblastic cells since they have the potential to express an osteoblastic phenotype when cultured under specific conditions. In addition, MEF has been employed to evaluate the biological behavior of materials for bone applications [86]. The cells were cultivated with standard techniques for cell culture. Manipulation of cell cultures was carried out in a biosafety cabinet (class II). The cells were cultured using DMEM (Dulbecco Modified Eagles Minimal Essential Medium) with pyruvate (1 mM) and 10% FBS (Fetal Bovine Serum, Gibco, USA), in physiological conditions (37 ºC and 5% CO_2).

Biocompatibility of graphene-coated samples was tested using liquid extract (indirect exposure) and direct contact (direct culture), both tests according to the instructions described in ISO 10993 part 5 “Tests for in vitro cytotoxicity” [87]. Extract media was obtained by incubating the uncoated porous substrates in cell culture medium at 37 °C for 24 h. This indirect test aims to simulate or exaggerate the clinical use conditions that allow determining the potential toxicological hazard without causing significant changes in the sample [87]. A direct contact experiment was performed directly seeding cells on graphene-coated samples to allow cell adhesion onto the surface. To perform both tests, the cells and cells on samples were cultured in 24-well plates (Falcon, Corning, USA) at $5x10^3$ cells/cm^2.

The viable biomass was quantified after 0, 1, 2, and 3 days of incubation using a commercial kit WST1 (Roche Diagnostics, Germany). Morphology of the cells was analyzed with epifluorescence microscopy using standard Rhodamine-Phalloidin and Hoechst staining (Invitrogen, Thermo Fisher Scientific, USA), which shows red and blue fluorescence in cytoplasm and nucleus, respectively.

2.4. Biostatistical analysis

All in-vitro experiments were performed in triplicate, with n=3 for each studied condition. Results were expressed as mean value ± standard deviation. In addition, the specific growth rates were calculated using the equation $\delta X/\delta t=\mu X$ (where μ is the specific growth rate, X is the biomass and *t* is time) and analyzed with ANOVA and Tukey's post-test via Statgraphics software. Significance was considered at p values of $p < 0.05$.

3. Results and Discussion

3.1. Characterization of the porous substrates

As previously mentioned, Ti-35Nb-29Ta-xMn (x: 2, 4, and 6 wt.%) alloys were chosen due to their promising mechanical properties and their expected biocompatibility. OM micrographs and SEM images of c.p. Ti and Ti-35Nb-29Ta-xMn porous samples obtained by space holders technique are depicted in Figure 2 and Figure S2. In general, the presence of macro and micropores distributed in a random and homogeneous way is observed [88]. In particular, samples of the Ti-35Nb-29Ta-4Mn alloy (Figure 2 (b) and (c)) present a higher concentration of micropores than the c.p. Ti sample (Figure 2 (a)) which exhibits a more homogeneous matrix, with a small percentage of micropores and higher densification. Nevertheless, when adding refractory alloying elements, such as Nb and Ta, higher sintering temperatures are required to

decrease the formation of micropores and to obtain a more densified matrix. SEM images also confirmed that samples with the same Mn content (4 wt.%), but different sintering temperatures (1200 °C and 1300 °C), do not show a significant difference in terms of porosity and pore size.

SEM images of 4 wt.% Mn foams (Figure 2 (d) and (e)) showed bimodal porous distribution composed of macropores with size in the range of 100 – 800 μm and micropores smaller than 20 μm are observed. The macro and micropores are uniformly distributed, exhibiting the typical irregular morphology produced by the space holder method [8, 89, 90]. Cell edges of macropores are irregular in thickness and present a random distribution, which may influence the mechanical properties of samples. Besides, this bimodal porous distribution is suitable for promoting bone ingrowth and vascularization [91].

In general, the macropores in the Ti-35Nb-29Ta-xMn samples exhibit rounded corners, as seen in Figure 2 (d) and (e). Rounded corners in porous structures contribute to prevent stress concentration and to reduce the probability of failure. Also, the presence of micropores is observed inside the cell walls and edges of macropores, as it is shown in Figure 2 (d) and (e). Similar results were reported for Ti-Nb-Zr foams by Rao et al. [92] and Ti-Mg foams by Wang et al. [88]. An important aspect of cell seeding/growth is the inner roughness of pores which can contribute to cell adhesion, as it was discussed before. The roughness of the inner pore surface can be controlled through the shape and size of the space holder, the amount of Ti, Nb, Ta and Mn powders, and the sintering time and temperature [55]. In this case a rough inner surface was found for both macro and micropores (see Figure 2 (f) and (g)).

The results of the Archimedes´ method and image analysis are summarized in the frequency distribution histograms of pore size for each wt.% Mn and sintering temperature (Figure 3). The image analysis information for each distribution is summarized in Table I, expressed in terms of mean value ± standard error (*). Interconnectivity is an important criterion used to evaluate porous implants for its role in nutrition delivery and body fluid transport [93, 94]. The total and

interconnected porosity of samples obtained by the Archimedes' method are, on average, 70% and 57%, respectively. The porosity measured by image analysis (P(IA)) is slightly lower than P(Arch) since only the results of surface porosity are considered. It is also observed that the porosity is greater than the space holder percentage. In the case of samples with 4 wt.% Mn, the porosity estimated by image analysis is about 50%. This aspect is important since the elements of the alloy are influencing the porosity in a significant way. Previous author´s work showed that, when using the space holder technique, porosities close to wt.% of the added spacer can be achieved [16, 22, 95].

Table I. Morphological parameters of pores.

Mn [wt.%]	Sintering Temperature [°C]	Total Porosity P(Arch) [%]	Interconnected Porosity Pint [%]	Porosity by Image Analysis (IA) [%]	Equivalent Diameter Deq (*) [μm]	Shape factor Ff	Pore distance λ [μm]
2	1200	70.2±0.0	54.2±0.2	63.0±4.9	181.3±13.7	0.68±0.29	7.3
	1300	69.2±0.1	50.8±0.4	62.4±5.6	201.7±15.7	0.80±0.24	9.6
4	1200	68.5±0.2	59.5±0.2	52.1±5.1	161.5±7.4	0.76±0.27	12.3
	1300	68.7±0.0	59.4±0.1	57.6±5.5	194.9±13.1	0.77±0.25	10.9
6	1200	71.2±0.2	57.3±0.0	66.2±3.4	183.3±11.4	0.81±0.24	6.4
	1300	70.8±0.3	62.0±0.4	67.2±3.9	192.3±20.2	0.76±0.26	7.3

The equivalent pore diameter (Deq) obtained by image analysis was between 162 and 202 μm, approximately. No significant effects of Mn content or sintering temperature on the pore diameter were found. Pore diameters obtained by different sintering temperatures and Mn contents are not statistically different ($p > 0.05$). The observed pore size distribution shows that 50-80% of the pores are between 100 and 200 μm size, 10-15% are around 400 μm size, whereas only 5% of the

pores are around 800 μm size. Interestingly, the formation of pores larger than 1200 μm for the 2 wt.% Mn and 6 wt.% Mn samples was observed. These larger isolated pores could be attributed to the initial size and possible interconnectivity between the particles. However, in specimens with 4 wt.% Mn, a maximum value of 800 μm pore size was obtained. This size is similar to the values obtained in commercial foams and trabecular bones [96].

The calculated pore shape factor (Ff) was 0.76 (Ff equal to 1 suggests a rounded pore). The statistical analysis (Tukey test) indicates that the influence of sintering temperature on Ff is statistically significant for samples with 2 wt.% Mn, with p-value < 0.05, whereas for 4 wt.% Mn and 6 wt.% Mn, the sintering temperature has little or no effect. Besides, there is a substantial difference between the shape factor values for the 2 wt.% Mn and 6 wt.% Mn samples sintered both at 1200°C and at 1300°C. However, when samples of 2 wt.% Mn and 4 wt.% are compared, this large difference can be only found in samples sintered at 1300°C.

The pore distance, λ, is used to determine the mean distance between pores. In this case, the calculated λ is between 7.3 and 12 μm, with values slightly higher for the 4 wt.% Mn sample. These λ values indicate that the pores are separated by distances that are on average less than their pore size (Figure 2 (d) and (e)). In this sense, the best result is the one obtained for 4 wt.% Mn specimens, while c.p. Ti sample showed an average value of 85 μm. This confirms what was observed in optical microscopy (Figure 2), where a difference in the porosity distribution and the mean free path between the pores was noticed. From this image analysis it can be inferred that 4 wt.% Mn samples present better results in terms of porosity control, pore morphology, and pore interconnectivity.

Ti alloy samples sintered at 1200 and 1300 °C were analyzed by X-ray diffraction (Figure 4) to identify Ti phases. Biesiekierski, et al. [34] have shown that Nb and Ta, which possess the same crystalline structure than Ti and show complete miscibility, are β-isomorphous elements. Although, Mn is a β-eutectoid element, i.e. it is not perfectly soluble in the Ti bulk, its eutectoid

effect could be reduced using a low percentage of Mn and the addition of isomorphous stabilizers [97]. XRD pattern analysis confirmed the presence of β-Ti phase (cubic structure) at room temperature, together with a small amount of α phase (hexagonal structure) for all Mn content and both sintering temperatures. Peaks corresponding to the β phase are large for samples sintered at 1200 ºC and, in some cases, they split as a consequence of an incomplete alloying process; thus, the more Mn content, the more evident this effect is. According to these results, the presence of β-isomorphous Nb and Ta promotes the stabilization of β-phase of Ti alloys samples at room temperature, despite the β-eutectoid nature of Mn. These results are confirmed by TEM measurements (Figure 5).

A TEM image of 4 wt.% Mn porous sample sintered at 1200 °C and the corresponding polycrystalline electron diffraction pattern are presented in Figure 5 (a). The multiple rings, most of which can be attributed to the β phase of titanium, revealed the polycrystalline nature of the sample. In Figure 5 (b), a high-resolution TEM (HR-TEM) micrograph of the same sample is shown. In the inset, the Fast Fourier Transform corresponding to the two different grains marked with a dashed square is displayed. Both can be unambiguously assigned to the BCC phase of titanium along the [001] and [011] zone axis.

XRD patterns and transmission electron microscopy confirm the presence of a β-phase matrix in Ti-35Nb-29Ta-xMn (x: 2, 4, and 6 wt.%) alloys. Despite the complexity of obtaining β-phase, it is possible to stabilize this phase at room temperature.

In a similar way, the β phase of the Ti-based alloy appears to be well formed at 1300 °C. According to the results obtained for both sintering temperatures, a solid solution is formed between Ti, Nb, Ta and Mn, during the sintering process. A brief inspection of phase diagrams shows that the binaries systems Ti-Nb [98] and Ti-Ta [98] present complete mutual solubility in the temperature range mentioned. Furthermore, for the Ti-Mn system [98], it is feasible to form a Ti-β solid solution with an amount of Mn between 18 to 30 wt.%. There are not reports in the

literature about the phase diagram of Ti-Nb-Ta-Mn and few reports regarding the phase diagram of Ti-Nb-Ta [99, 100].

The mechanical response of porous samples was analyzed by uniaxial compression tests, performed on Ti-35Nb-29Ta-xMn (2, 4, and 6 wt.% Mn) specimens sintered at 1200 °C and 1300 °C, and the results were compared with previous author's works [21, 55, 95]. The results of the compression tests and stress–strain curves, are presented in Figure 6. In general, the curves indicate an elastic linear behavior followed by a flatter plateau-like region starting around 50 MPa. The Ti-35Nb-29Ta-4Mn samples sintered at 1200 °C exhibited the best mechanical performance under compression stress. This aspect could be related to the results observed in microstructural characterization and image analysis, where the porosity distribution and morphology present the best results.

The observed mechanical properties of Ti-based β alloys for all Mn contents are summarized in Table II. The compression test results of the foams showed Young´s modulus (E_c) in the range of 9-12 GPa. Also, Young's moduli estimated by the Nielsen equation ($E_{Nielsen}$) [80] showed values very similar to those achieved by the compression test. The values are in the admissible range for bone tissue replacement (3-30 GPa). There are no significant differences between the E_c or $E_{Nielsen}$ for c.p Ti and Ti-Nb-Ta-Mn samples. Furthermore, yield strength (σ_y) was calculated according to the criterion proposed by R. M. Christensen [79], obtaining values between 30 MPa and 67 MPa. According to the results, the sample with 4 wt.% Mn sintered at 1200 °C exhibits the highest σ_y value and compression stress (69 MPa and 98 MPa, respectively). This sample showed a superior capacity of energy absorption in the compression test (area under the curve), which provides a better toughness (Figure 6). In the 4 wt.% Mn samples, pores are smaller than 800μm (Figure 3), the lowest value for the studied samples. Besides, λ is higher than those achieved for samples with other wt% Mn contents. These aspects are particularly relevant in mechanical performance, because of the effect of the pore-size distribution on sample strength.

An increase of λ enhances the fraction of the effective strength area and, consequently, the mechanical strength is improved. The plastic behavior of these materials was controlled by the collapse of pores walls and not by the strain hardening. In any case, obtained specimens showed better mechanical strength and ductility than c.p. Ti grade 4 foams with similar porosity, as observed in Table II [95]. Therefore, even if both materials (Ti and Ti alloy) were completely dense, Ti-35Nb-29Ta-xMn samples should have better mechanical response than c.p Ti samples in terms of mechanical strength and ductility, and less stress shielding because of the lower discrepancy with the cortical or cancellous bone tissue (3-30 GPa).

Table II. Mechanical properties for porous Ti c.p. and Ti-Nb-Ta-Mn alloys. **Note:** *Ref [88] and ** Christensen's [72].

		Sintering Temperature [°C]	Total Porosity [%]	Young's Modulus [GPa]		σ_y estimated** [MPa]	Maximum Compression Strain [mm/mm]
				E_c	$E_{Nielsen}$		
	c.p.Ti*	1250	66	2.6	10.9	29.0	0.04
Mn [wt.%]	2	1200	70.2	9.8	10.5	41.6	16.9
		1300	69.2	10.1	12.6	52.7	24.9
	4	1200	68.5	9.2	12.9	67.5	21.3
		1300	68.7	9.3	12.7	42.3	12.4
	6	1200	71.2	11.8	11.1	30.4	14.6
		1300	70.8	9.8	11.0	43.3	16.2

Regardless of the type of titanium alloy used, the space holder technique is effective to reach porous structures with pore size and interconnectivity degree needed to benefit the physiological fluid entrance and the subsequent growth of bone tissue inside the implant. Porosity reduces

Young's modulus, but also, high porosity levels compromise the tribomechanical and corrosion behavior of the materials. In the case of β alloys, the values required for cortical bone tissue could be achieved by lowering the porosity that translates into less mechanical performance loss. For the obtained β Ti alloys, Young's modulus was reduced, the ductility was improved, and the yield strength was found close to trabecular bones [96], as shown in Figure 5. Hence, the synthesized Ti alloy foams present a promising mechanical behavior for bone replacement applications, in contrast to the results obtained in previous studies [55]. The observed Young's modulus value of porous Ti-35Nb-29Ta-4Mn samples, with values ranging between 8.0 and 9.3 GPa, and pore size values between 100 and 800 μm, are closer to those of the trabecular bone [23, 30] and similar to the ones found in previous studies on other Ti alloys (Table III).

Table III summarizes the physical and mechanical properties of porous metals, some commercially available alloys [101-103], and trabecular bone [104]. Besides the above-mentioned potential of Ti-35Nb-29Ta-4Mn alloy for bone replacement, it is expected that the reduction in processing time achieved in this work will impact on the overall costs of the manufacturing route, making more likely the adoption, commercialization and wide-scale application of this technology.

Table III. Physical and mechanical properties comparison of commercial porous metals and trabecular bone with porous Ti alloys obtained in this work and other authors´ studies [8, 55, 96, 101-103, 105-107]. *Measured by Ultrasound technique, **processed by mechanical alloying and sintering.

	Composition	Total Porosity [%]	Pore Size [μm]	Yield Strength [MPa]	Young's Modulus [GPa]
Biofoam™	50% and 50% Polysaccharides high	60-70	478-	55-70	2.5-3.0

	molecular weight proteins		578		
Regenerex™	Matrix enhanced with thymosin β4 (Tβ4)	67	100-600	-	1.6
Trabecular Metal™	Carbon foam infiltrated with tantalum	75-85	550	35-51	2.5-3.9
Cachinho et al	c.p Ti	75	100-600	-	0.3
Jia et al	c.p Ti	79	370-600	21	0.9
Torres et al [+]	c.p Ti	65-68	50-300	2-31	9.2-11.2*
Aguilar et al**	Ti–34Nb–29Ta–xMn	50	100-600	22-55	27.0-33.0
This study	4 wt.% Mn	69-72	100-800*	25-68	8.0-9.3
Trabecular bone	Matrix 30% (ossein (collagen fibers)) Bound minerals 70% (Calcium hydroxyapatite)	70-80	400-700	2-12	0.1-0.5

Although from the mechanical and structural point of view the Ti-35Nb-29Ta-4Mn alloy confirmed to be suitable for bone-replacement applications when it comes to corrosion resistance, potential for osseointegration and protection against biofilm formation, additional strategies need to be explored.

In this context, nanoscale surface modification has emerged as a powerful tool to control cellular behavior and to develop biomimetic surfaces, since it has been confirmed that material-host tissue interactions are principally governed by nanometric phenomena [108, 109]. To improve the biological response of obtained surfaces, the use of single-layer graphene has been explored, a nanostructured coating that has been reported to be cytocompatible [81, 110], to suppress biofilm formation [82] and to protect metals from electrochemical corrosion [111] and

microbial-induced corrosion [83, 84]. Besides, this one-atom-thick material presents a good adhesion to metallic surfaces [112], which can be relevant, considering several reports on the detachment of hydroxyapatite from the Ti surface [113].

3.2. Characterization of graphene coatings

Before transfer SLG onto the Ti substrate, the graphitic quality and atomic resolved imaging of CVD graphene grown on Cu was characterized by Raman spectroscopy and STM (Figure 7). Large-scale STM tomography (Figure 7 (a)) and characteristic fingerprint of single-layer graphene (honeycomb pattern) were observed through atomic-resolved topographies. A hexagonal structure with around 2.4 Å lattice distance was found (Figure 7 (b)), in agreement with expected values for this graphitic material [84, 114]. CVD graphene transferred onto SiO_2 displays sharp G (1584 cm^{-1}) and 2D (2680–2693 cm^{-1}) bands. The G band indicates the order and purity structure of graphite sheets. The 2D band is the characteristic peak of the graphene structure. It is known that the ratio I_{2D}/I_G of the intensities of the bands 2D and G are dependent on the number of graphene layers [83, 105, 115]. The ratio I_{2D}/I_G~ 2-3 is for single-layer graphene, $I_{2D}/I_G > 1$ for bilayer graphene, and $I_{2D}/I_G < 1$ for multilayer one (graphite). The graphene sample transferred on SiO_2 exhibits a ratio $I_{2D}/I_G > 2$, Figure 7 (c), which is consistent with single-layer graphene [84, 114]. Raman spectroscopy was performed to confirm the presence of the SLG coating onto the Ti-Nb-Ta-Mn porous substrate and to evaluate the quality of the transfer process. Figure 7 (d) shows Raman spectra of the CVD single-layer graphene supported on the substrates, suspended over a pore, and on a flat area between pores. The micrographs of the analyzed zones are shown in Figure 7 (e) and (f). The intensity ratio I_{2D}/I_G associated with suspended graphene is ~2.5, significantly higher than that for the graphene on the solid surface of the porous substrate, $I_{2D}/I_G \approx 1.5$. This change of the intensity ratio I_{2D}/I_G is due to the Etalon effect [116] of the pore surface under graphene: both surfaces are reflective and the

signal obtained for the Raman analysis from the graphene interferes with the one reached from the pore surface. In addition, this constructive interference between the suspended graphene and the inner surface of the pore also produces a strong background signal (See Figure 7d and Figure S3) which has been reported for suspended graphene on TEM grids [116]. The phenomenon is not observed for the smooth surface due to the proximity between layers. The observed shifting in the position of 2D and G bands is probably related to the strain induced on the graphene [117] due to the roughness of the surface and the porosity. Also, a defect band is observed on the spectra obtained on the coating supported on the foam, caused by the wrinkles on the coating, which can be seen in Figure 7 (e) and Figure 8 (c).

The morphology of graphene coating transferred onto Ti alloy substrates was studied through OM and SEM (Figure 8). It has been reported that bioactive coatings such as graphene, enhance the formation of calcium phosphates (bone) [62, 72] and improve the cellular adhesion due to the biofunctionalization of the surface. According to these images, coating presents a good graphene coverage of the porous Ti substrate, both flat areas and pores (Figure 8 (a) and (c)). Graphene coating is entirely suspended over the pores (areas marked with the arrows) when pores are smaller than ~400 μm (Figure 8 (d)). However, for larger pores the coating integrity is affected, leading to the presence of holes that leave these large pores exposed (Figure 8 (b) and (d)).

This damage is presumably connected with some intrinsic aspects of the transfer process such as (a) the pressure resulting from the vaporization inside the pore of the remnant fluid used during transfer procedure or (b) the stress introduced in the coating when the coated sample is baked to improve coating adhesion. The presence of PMMA residues from other transference process is observed as stains using bright field in Figure 8 (a) and dark field in Figure 8 (b) [116, 117]. It is a consequence of the low-cost method used here for graphene transfer. In any case, PMMA is used on biomedical applications because of its good biocompatibility [83, 115] and despite some concerns such as its cytotoxicity [118], the quantity of PMMA found here is very

low and is expected to not interfere in graphene performance. Finally, the SEM image of coated substrates is presented in Figure 8 (c) confirming the presence of graphene wrinkles at the SLG coating surface, produced during the transfer process [119].

3.3. Cytotoxicity and biocompatibility test

Results of cell growth for the 72 hours' biocompatibility tests (uncoated and coated samples) are depicted in Figure 9. MEF cells cultured on the graphene-coated samples, showed an exponential growth phase similar to that obtained in fresh medium, indicating that SLG is an optimal material for MEF cell growth. However, cells directly seeded onto the uncoated substrate did not grow, suggesting that they cannot adhere to the metallic material without surface treatment. According to these results, since the Ti alloy does not exhibit cytotoxicity but shows poor cell adhesion, it can be treated by using a SLG coating to promotes cell growth. At 72h, the results show a reduced cell proliferation on graphene-coated materials compared to the fresh medium. This behavior is similar to the one observed when cells begin the osteoblastic differentiation process which decreases proliferation rate. Another aspect to be considered is the intrinsic physical damage of SLG coating when it is transferred using PMMA-assisted method. This might lead to a partially covered substrate that may influence the cell growth rate. However, as previously mentioned, the cell proliferation values are reasonable from a biological point of view, suggesting that SLG improves the cell growth and adhesion of cells on the porous Ti-35Nb-29Ta-4Mn substrate.

The morphology of the cells at 24, 48, and 72 hours is shown in Figure S4. The cells grown on the graphene-coated samples presented a spherical morphology at 24 hours, and some of them already begin to show a typical fibroblastic cell morphology when cells are adhering to the surface. At 72 hours, the cell's elongated shape, standard in fibroblasts, was observed and a larger

number of cells in stage of mitosis can be found. This indicates an active proliferation process with evident cellular connections (cell-cells and cell-surface) through cytoplasmic elongations. The same pattern is observed on the cells grown on polystyrene surface and in fresh medium (Figure S4).

For cells grown in liquid extract, the changes in cell morphology occur more slowly. At 24 hours, they have a spherical shape, but the standard fibroblastic form is not observed at 72 hours (Figure S4). This indicates that liquid extract affects cell behavior, although without clear evidence of cytotoxicity. At 72h we observed a similar number of cells with rounded shape (that is usually associated to lower adhesion to the surface), and some cells with the typical pinoptic nucleus related to cell death (apoptosis).

3.4. Results of biostatistical analysis

Biostatistical analysis show that specific growth rate (μ) is different in terms of culture type (Figure 8). Consequently, the type of culture affects cell growth ($p < 0.05$, ANOVA).

The specific growth rate (μ) of the cells cultured with liquid extract (0.76 ± 0.11 [d^{-1}]) as compared to cells cultured in fresh medium ($\mu=0.79\pm0.04$), is not significantly different ($p>0.05$). The cells with liquid extract show proliferation in the exponential phase at a rate similar to that of the fresh medium.

The cells onto graphene-coated substrates grew significantly faster ($\mu=0.66 \pm 0.11$ [d^{-1}], p-value <0.05) than cells directly cultured on uncoated titanium substrates, that did not adhere or growth ($\mu=0$, (p-value > 0.05)).

These results suggest that the single-layer graphene coating favors the cell adhesion and growth on the surface of porous Ti-35Nb-29Ta-4Mn samples, improving the osseointegration. This outstanding behavior might be connected to the modification of interactions between graphene and cells. Graphene coating has been used to suppress microbial induced corrosion of metals [83, 114] by creating an impermeable layer that prevents the release of metal ions from underneath

metallic materials exposed to biological environments. This might be the case here, where a transferred single-layer graphene coating could be acting as a barrier between cells in the growth medium and the porous Ti alloy. Although the SLG coating usually presents physical damage, intrinsic to the PMMA-assisted transfer process, its effectiveness as an ionic barrier has been proven before for transferred SLG onto other metallic substrates [83]. Such impermeability is, of course, lower than in the case of SLG grown on the metallic sample, but still between 50 and 80% in the case of graphene-coated Ni [83], where metallic ion transfer to growth medium was quantified. In this context, one possible interpretation of the observed results is connected to the impermeability of SLG coating (pore size 64pm) [83, 114] to metallic ions with bigger effective ionic radii (Nb (68pm) [120], Ta (68pm) [121], and Mn (66pm) [122]). The nanostructured coating might be preventing the contact between these metallic elements and the MEF cells, but additional spectroscopic measurements are required to quantify this effect. In addition, for the MEF experiments carried out in this work, it is important to highlight that, although the SLG coating is covering only one face of Ti alloy samples, this is exactly the face where the cells were cultured, preventing the interference in the cell-surface interaction coming from any of the other uncoated faces of the metallic sample.

As has been reported for other nano featured titanium surfaces, nanoscale topography changes due to the graphene coating might be determining an increase in the adsorption of proteins related to surface bioactivity [123]. However, further experiments and calculations need to be carried out to understand the contribution of other phenomena such as electrostatic interactions and surface energy to cellular specific functions, such as adhesion, proliferation, and differentiation.

4. Conclusion

In this study, a novel approach to develop biocompatible porous Ti alloys with enhanced mechanical and biological performance is presented. Mechanical properties were improved by

searching for the proper crystalline phase of the Ti samples whereas biological performance was increased by introducing nanostructured coatings.

The porous Ti-35Nb-29Ta-xMn (x: 2, 4, 6 wt.%) alloy samples, with a high level of porosity (69-72%) and pore size ranging between 100-800 μm, were obtained by a powder metallurgy process. It was found that a 4wt. % Mn content favors the presence of the β-Ti phase. This aspect, added to the influence of porosity and pore size in this alloy, leads to Young's modulus (8.0-9.3 GPa) closer to trabecular bone. Although cytotoxicity test showed that Ti-35Nb-29Ta-4Mn is not cytotoxic, this uncoated porous material presented neither significant cell adhesion nor proliferation.

To improve biocompatibility, the use of CVD single-layer graphene coatings was explored. According to results obtained from this research, SLG coating favors cell growth and adhesion to the porous Ti-35Nb-29Ta-4Mn substrate. One possible interpretation of these results is connected to the previously reported impermeability of graphene coating to metallic ions, which in this system might be preventing the contact between Mn, Ta and Nb elements and the MEF cells, favoring its growth. Although this "barrier" performance has been previously proven for transferred graphene onto metallic substrates, further measurements of the released Ta, Nb and Mn ions are required to quantify this phenomenon. In addition, further high-resolved structural studies will help to understand the effect of the nanoscale surface morphology of the graphene coating on cell growth and proliferation.

Corresponding Author

e-mail addresses: sheila.lascano@usm.cl (S. Lascano)

Author Contributions

The manuscript was written with the contributions of all authors. All authors have given approval to the final version of the manuscript. **Sheila Lascano**: Investigation, Writing- Review & Editing,

Funding acquisition, **Ricardo Chávez-Vásconez**: Investigation, Formal analysis, Writing, **Daniela Muñoz-Rojas**: Investigation, Formal analysis, **Juliet Aristizabal**: Investigation, Writing- Original Draft, **Bárbara Arce**: Investigation, **Carolina Parra**: Investigation, Resources, Writing- Review & Editing, **Cristian Acevedo**: Investigation, Resources and Writing, **Nicole Orellana**: Investigation, Formal Analysis, **Mauricio Reyes-Valenzuela**: Investigation, Formal Analysis, **Francisco José Gotor**: Formal Analysis, Review & Editing, **Cristina Arévalo**: Investigation, Resources, Writing- Review & Editing, **Yadir Torres**: Investigation, Review & Funding acquisition

Funding Sources

This work was supported by the Agencia Nacional de Investigación y Desarrollo (ANID) of Chile government [grant number Fondecyt 11160865, Fondecyt 1180702 and FONDEQUIP EQM150101], by the regional government from Andalusia through FEDER- Junta de Andalucía Research Project, Ref. US-1259771 (Modelling and implementation of the freeze casting technique: gradients of porosity with a tribomechanical equilibrium and electro- stimulated cellular behavior) and the Ministerio de Ciencia e Innovación of Spain under the grant PID2019-109371GB-I00

Acknowledgments

The authors thank Dr. Mercedes Giner García (Departamento de Citología e Histología) for her support in the analysis of biological behavior and the laboratory technicians Jesus Pinto at Universidad de Sevilla (Spain), María del Carmen Jiménez de Haro and José María Martínez Blanes (CSIC), Claudio Aravena and Gabriel Cornejo at Universidad Técnica Federico Santa María (Chile) for their support carrying out the microstructure characterization and mechanical

testing, and Francisco Varela for his support in FIB (experimental facilitates at CITIUS,

Universidad de Sevilla, VI PPIT-2019-I.5 C. Arévalo).

References

[1] M. Kaur, K. Singh, Review on titanium and titanium based alloys as biomaterials for orthopaedic applications, Mater. Sci. Eng., C. 102 (2019) 844-862. https://doi.org/10.1016/j.msec.2019.04.064.

[2] Y. Torres, P. Trueba, J. Pavón, I. Montealegre, J. Rodríguez-Ortiz, Designing, processing and characterisation of titanium cylinders with graded porosity: an alternative to stress-shielding solutions, Mater & Des. 63 (2014) 316-324. https://doi.org/10.1016/j.matdes.2014.06.012.

[3] L.C. Zhang, L.Y. Chen, A review on biomedical titanium alloys: recent progress and prospect, Advanced Engineering Materials. 21 (2019) 1801215. https://doi.org/10.1002/adem.201801215.

[4] M. Niinomi, M. Nakai, J. Hieda, Development of new metallic alloys for biomedical applications, Acta Biomater. 8 (2012) 3888-3903. https://doi.org/10.1016/j.actbio.2012.06.037.

[5] F. Schmidutz, Y. Agarwal, P.E. Müller, B. Gueorguiev, R.G. Richards, C.M. Sprecher, Stress-shielding induced bone remodeling in cementless shoulder resurfacing arthroplasty: a finite element analysis and in vivo results, J Biomech. 47 (2014) 3509-3516. https://doi.org/10.1016/j.jbiomech.2014.08.029.

[6] Y. Torres, J.J. Pavón, J.A. Rodríguez, Processing and characterization of porous titanium for implants by using NaCl as space holder, J. Mater. Proc. Technol. 212 (2012) 1061-1069. https://doi.org/10.1016/j.jmatprotec.2011.12.015.

[7] X. Wang, S. Xu, S. Zhou, W. Xu, M. Leary, P. Choong, M. Qian, M. Brandt, Y.M. Xie, Topological design and additive manufacturing of porous metals for bone scaffolds and orthopaedic implants: A review, Biomater. 83 (2016) 127-141. https://doi.org/10.1016/j.biomaterials.2016.01.012.

[8] Y. Torres, S. Lascano, J. Bris, J. Pavón, J.A. Rodriguez, Development of porous titanium for biomedical applications: A comparison between loose sintering and space-holder techniques, Mater. Sci. Eng., C. 37 (2014) 148-155. https://doi.org/10.1016/j.msec.2013.11.036.

[9] L. Zhou, T. Yuan, J. Tang, J. He, R. Li, Mechanical and corrosion behavior of titanium alloys additively manufactured by selective laser melting – A comparison between nearly β titanium, α titanium and α + β titanium, Opt. & Laser Technol. 119 (2019) 105625. https://doi.org/10.1016/j.optlastec.2019.105625.

[10] X. Miao, D. Sun, Graded/Gradient Porous Biomaterials, Mater. 3 (2010) 26-47. https://doi.org/10.3390/ma3010026.

[11] J. Parthasarathy, B. Starly, S. Raman, A. Christensen, Mechanical Evaluation of Porous Titanium (Ti6Al4V) structures With Electron Beam Melting (EBM), J Mech Behav Biomed Mater. 3 (2010) 249-259. https://doi.org/10.1016/j.jmbbm.2009.10.006.

[12] S.M. Oppenheimer, D.C. Dunand, Porous NiTi by creep expansion of argon-filled pores, Mater. Sci. Eng., A. 523 (2009) 70-76. https://doi.org/10.1016/j.msea.2009.05.045.

[13] R. Orrù, R. Licheri, A.M. Locci, A. Cincotti, G. Cao, Consolidation/synthesis of materials by electric current activated/assisted sintering, Mater. Sci. Eng., R Rep. 63 (2009) 127-287. https://doi.org/10.1016/j.mser.2008.09.003.

[14] Z. Esen, E.T. Bor, Characterization of loose powder sintered porous titanium and Ti6Al4V alloy, Turk. J. Eng. Environ. Sci. 33 (2009) 207-219. https://doi:10.3906/muh-0906-41.

[15] C.E. Wen, M. Mabuchi, Y. Yamada, K. Shimojima, Y. Chino, T. Asahina, Processing of biocompatible porous Ti and Mg, Scr. Mater. 45 (2001) 1147-1153. https://doi.org/10.1016/S1359-6462(01)01132-0.

[16] S. Lascano, C. Arévalo, I. Montealegre-Melendez, S. Muñoz, J.A. Rodriguez-Ortiz, P. Trueba, Y. Torres, Porous Titanium for Biomedical Applications: Evaluation of the Conventional Powder Metallurgy Frontier and Space-Holder Technique, Appl. Sci. 9 (2019) 982. https://doi.org/10.3390/app9050982.

[17] N. Wenjuan, B. Chenguang, Q. GuiBao, W. Qiang, Processing and properties of porous titanium using space holder technique, Mater. Sci. Eng., A. 506 (2009) 148-151. https://doi.org/10.1016/j.msea.2008.11.022.

[18] D. Dunand, Processing of titanium foams, Adv. Eng. Mater. 6 (2004) 369-373. https://doi.org/10.1002/adem.200405576.

[19] R. Singh, P.D. Lee, R.J. Dashwood, T.C. Lindley, Titanium foams for biomedical applications: a review, Mater. Technol. 25 (2010) 127-136. https://doi.org/10.1179/175355510X12744412709403.

[20] S. Kashef, A. Asgari, T.B. Hilditch, W. Yan, V.K. Goel, P.D. Hodgson, Fatigue crack growth behavior of titanium foams for medical applications, Mater. Sci. Eng., A. 528 (2011) 1602-1607. https://doi.org/10.1016/j.msea.2010.11.024.

[21] Y. Torres, J.A. Rodríguez, S. Arias, M. Echeverry, S. Robledo, V. Amigó, J.J. Pavón, Processing, Characterization and biological testing of porous titanium obtained by space-holder technique, J. Mater. Sci. 47 (2012) 6565-6576. https://doi.org/10.1007/s10853-012-6586-9.

[22] A. Civantos, M. Giner, P. Trueba, S. Lascano, M.-J. Montoya-García, C. Arévalo, M.Á. Vázquez, J.P. Allain, Y. Torres, In Vitro Bone Cell Behavior on Porous Titanium Samples: Influence of Porosity by Loose Sintering and Space Holder Techniques, Metals. 10 (2020) 696. https://doi.org/10.3390/met10050696.

[23] G. Kotan, A. Bor, Production and Characterization of High Porosity Ti-6Al-4V Foam by Space Holder Technique in Powder Metallurgy, Turk. J. Eng. Environ. Sci. 31 (2007) 149-156.

[24] Y.Y. Zhao, T. Fung, L.P. Zhang, F.L. Zhang, Lost carbonate sintering process for manufacturing metal foams, Scr. Mater. 52 (2005) 295-298. https://doi.org/10.1016/j.scriptamat.2004.10.012.

[25] A. Manonukul, N. Muenya, F. Léaux, S. Amaranan, Effects of replacing metal powder with powder space holder on metal foam produced by metal injection moulding, J. Mat. Process. Technol. 210 (2010) 529-535. https://doi.org/10.1016/j.jmatprotec.2009.10.016.

[26] T. Fengqiu, H. Fudouzi, T. Uchikoshi, Y. Sakka, Preparation of porous materials with controlled pore size and porosity, J. Eur. Ceram. Soc. 24 (2004) 341-344. https://doi.org/10.1016/S0955-2219(03)00223-1.

[27] M. Guden, E. Celik, E. Akar, S. Cetiner, Compression testing of a sintered Ti6Al4V powder compact for biomedical applications Mater. Charact. 54 (2005) 399-408. https://doi.org/10.1016/j.matchar.2005.01.006.

[28] R. Surace, L.A.C. De Filippis, A.D. Ludovico, G. Boghetich, Influence of processing parameters on aluminium foam produced by space holder technique, Mater. Des. 30 (2009) 1878-1885. https://doi.org/10.1016/j.matdes.2008.09.027.

[29] Y. Bing, D. Dunand, Titanium foams produced by solid-state replication of NaCl powders, Mater. Sci. Eng., A. 528 (2010) 691-697. https://doi.org/10.1016/j.msea.2010.09.054.

[30] M. Geetha, A.K. Singh, R. Asokamani, A.K. Gogia, Ti based biomaterials, the ultimate choice for orthopaedic implants–a review, Prog. Mater. Sci. 54 (2009) 397-425. https://doi.org/10.1016/j.pmatsci.2008.06.004.

[31] R.M. Pilliar, Metallic biomaterials, in: R. Narayan (Ed.) Biomedical Materials, Springer, Boston, MA, 2009, pp. 41-81.

[32] M.A.-H. Gepreel, M. Niinomi, Biocompatibility of Ti-alloys for long-term implantation, J Mech Behav Biomed Mater. 20 (2013) 407-415. https://doi.org/10.1016/j.jmbbm.2012.11.014.

[33] D. Correa, F. Vicente, T. Donato, V. Arana-Chavez, M. Buzalaf, C.R. Grandini, The effect of the solute on the structure, selected mechanical properties, and biocompatibility of Ti–Zr system alloys for dental applications, Mater. Sci. Eng., C. 34 (2014) 354-359. https://doi.org/10.1016/j.msec.2013.09.032.

[34] A. Biesiekierski, J. Wang, M.A.-H. Gepreel, C. Wen, A new look at biomedical Ti-based shape memory alloys, Acta Biomater. 8 (2012) 1661-1669. https://doi.org/10.1016/j.actbio.2012.01.018.

[35] D. Kuroda, M. Niinomi, M. Morinaga, Y. Kato, T. Yashiro, Design and mechanical properties of new β type titanium alloys for implant materials, Materials Science and Engineering: A. 243 (1998) 244-249. https://doi.org/10.1016/S0921-5093(97)00808-3.

[36] Y. Okazaki, Y. Ito, K. Kyo, T. Tateishi, Corrosion resistance and corrosion fatigue strength of new titanium alloys for medical implants without V and Al, Materials Science and Engineering: A. 213 (1996) 138-147. https://doi.org/10.1016/0921-5093(96)10247-1.

[37] Y. Chen, Z. Xu, C. Smith, J. Sankar, Recent advances on the development of magnesium alloys for biodegradable implants, Acta Biomater. 10 (2014) 4561-4573. https://doi.org/10.1016/j.actbio.2014.07.005.

[38] T. Hanawa, Materials for metallic stents, Journal Artif Organs. 12 (2009) 73-79. https://doi.org/10.1007/s10047-008-0456-x.

[39] B. Boyce, J. Byars, S. McWilliams, M. Mocan, H. Elder, I. Boyle, B. Junor, Histological and electron microprobe studies of mineralisation in aluminium-related osteomalacia, Journal of clinical pathology. 45 (1992) 502-508. http://dx.doi.org/10.1136/jcp.45.6.502.

[40] R. Koster, D. Vieluf, M. Sommerauer, Nickel and molybdenum contact allergies in patients with coronary in-stent restenosis, ACC Current J. Rev. 3 (2001) 62. https://doi.org/10.1016/S0140-6736(00)03262-1.

[41] P.C. Schalock, T. Menné, J.D. Johansen, J.S. Taylor, H.I. Maibach, C. Lidén, M. Bruze, J.P. Thyssen, Hypersensitivity reactions to metallic implants–diagnostic algorithm and suggested patch test series for clinical use, Contact dermatitis. 66 (2012) 4-19. https://doi.org/10.1111/j.1600-0536.2011.01971.x.

[42] C. Cui, B. Hu, L. Zhao, S. Liu, Titanium alloy production technology, market prospects and industry development, Mater. Des. 32 (2011) 1684-1691. https://doi.org/10.1016/j.matdes.2010.09.011.

[43] E.-S. Kim, Y.-H. Jeong, H.-C. Choe, W.A. Brantley, Formation of titanium dioxide nanotubes on Ti–30Nb–xTa alloys by anodizing, Thin Solid Films. 549 (2013) 141-146. https://doi.org/10.1016/j.tsf.2013.08.058.

[44] S. Acharya, A.G. Panicker, D.V. Laxmi, S. Suwas, K. Chatterjee, Study of the influence of Zr on the mechanical properties and functional response of Ti-Nb-Ta-Zr-O alloy for orthopedic applications, Mater & Des. 164 (2019) 107555. https://doi.org/10.1016/j.matdes.2018.107555.

[45] R. Schmidt, S. Pilz, I. Lindemann, C. Damm, J. Hufenbach, A. Helth, D. Geissler, A. Henss, M. Rohnke, M. Calin, M. Zimmermann, J. Eckert, M.H. Lee, A. Gebert, Powder metallurgical processing of low modulus β-type Ti-45Nb to bulk and macro-porous compacts, Powder Technol. 322 (2017) 393-401. https://doi.org/10.1016/j.powtec.2017.09.015.

[46] E. Chicardi, C. Aguilar, M.J. Sayagués, C. García-Garrido, Influence of the Mn content on the TiNbxMn alloys with a novel fcc structure, J. Alloy Compd. 746 (2018) 601-610. https://doi.org/10.1016/j.jallcom.2018.02.306.

[47] S. Xueqing, Y. Zhang, Y. Jiang, Z. Rong, Corrosion Behavior of Ti-35Nb-7Zr-5Ta Alloy Prepared by Spark Plasma Sintering in Hank's Artificial Body Fluid, Corros. Sci. Prot. Technol. 28 (2017) 543-548. https://doi.org/10.11903/1002.6495.2016.042.

[48] L.M. Zou, C. Yang, Y. Long, Z.Y. Xiao, Y.Y. Li, Fabrication of biomedical Ti–35Nb–7Zr–5Ta alloys by mechanical alloying and spark plasma sintering, Powder Metall. 55 (2012) 65-70. https://doi.org/10.1179/1743290111Y.0000000021.

[49] M. Hendrickson, S. Mantri, Y. Ren, T. Alam, V. Soni, B. Gwalani, M. Styles, D. Choudhuri, R. Banerjee, The evolution of microstructure and microhardness in a biomedical Ti–35Nb–7Zr–5Ta alloy, J. Mater. Sci. 52 (2017) 3062-3073. https://doi.org/10.1007/s10853-016-0591-3.

[50] M. Abdel-Hady, K. Hinoshita, M. Morinaga, General approach to phase stability and elastic properties of β-type Ti-alloys using electronic parameters, Scr. Mater. 55 (2006) 477-480. https://doi.org/10.1016/j.scriptamat.2006.04.022.

[51] I. Kohlstadt, Scientific evidence for musculoskeletal, bariatric, and sports nutrition, CRC Press, 2006.

[52] R. Nicula, F. Lüthen, M. Stir, B. Nebe, E. Burkel, Spark plasma sintering synthesis of porous nanocrystalline titanium alloys for biomedical applications, Biomol. Eng. 24 (2007) 564-567. https://doi.org/10.1016/j.bioeng.2007.08.008https://doi.org/10.1016/j.bioeng.2007.08.008.

[53] S. Ehtemam-Haghighi, H. Attar, M.S. Dargusch, D. Kent, Microstructure, phase composition and mechanical properties of new, low cost Ti-Mn-Nb alloys for biomedical applications, J. Alloy. Compd. 787 (2019) 570-577. https://doi.org/10.1016/j.jallcom.2019.02.116.

[54] C. Guerra, M. Sancy, M. Walczak, C. Martínez, A. Ringuedé, M. Cassir, J. Han, K. Ogle, H.G. de Melo, V. Salinas, Effect of added porosity on a novel porous Ti-Nb-Ta-Fe-Mn alloy exposed to simulated body fluid, Mater. Sci. Eng., C. 111 (2020) 110758. https://doi.org/10.1016/j.msec.2020.110758.

[55] C. Aguilar, C. Guerra, S. Lascano, D. Guzman, P.A. Rojas, M. Thirumurugan, L. Bejar, A. Medina, Synthesis and characterization of Ti–Ta–Nb–Mn foams, Mater. Sci. Eng., C. 58 (2016) 420-431. https://doi.org/10.1016/j.msec.2015.08.053.

[56] A. Civantos, C. Domínguez, R.J. Pino, G. Setti, J.J. Pavon, E. Martínez-Campos, F.J.G. Garcia, J.A. Rodriguez, J.P. Allain, Y. Torres, Designing bioactive porous titanium interfaces to balance mechanical properties and in vitro cells behavior towards increased osseointegration, Surf Coat Technol. . 368 (2019) 162-174. https://doi.org/10.1016/j.surfcoat.2019.03.001.

[57] M. Takemoto, S. Fujibayashi, M. Neo, J. Suzuki, T. Kokubo, T. Nakamura, Mechanical properties and osteoconductivity of porous bioactive titanium, Biomater. 26 (2005) 6014-6023. https://doi.org/10.1016/j.biomaterials.2005.03.019.

[58] A. Scislowska-Czarnecka, E. Menaszek, B. Szaraniec, E. Kolaczkowska, Ceramic modifications of porous titanium: effects on macrophage activation, Tissue Cell. 44 (2012) 391-400. https://doi.org/10.1016/j.tice.2012.08.002.

[59] S. Kumar, M. Nehra, D. Kedia, N. Dilbaghi, K. Tankeshwar, K.-H. Kim, Nanotechnology-based biomaterials for orthopaedic applications: Recent advances and future prospects, Mater. Sci. Eng., A. 106 (2020) 110154. https://doi.org/10.1016/j.msec.2019.110154.

[60] S.Y. Bhong, N. More, M. Choppadandi, G. Kapusetti, Review on carbon nanomaterials as typical candidates for orthopaedic coatings, SN Appl. Sci. 1 (2019) 76. https://doi.org/10.1007/s42452-018-0082-z.

[61] M. Gu, L. Lv, F. Du, T. Niu, T. Chen, D. Xia, S. Wang, X. Zhao, J. Liu, Y. Liu, Effects of thermal treatment on the adhesion strength and osteoinductive activity of single-layer graphene sheets on titanium substrates, Sci. Rep. 8 (2018) 1-15. https://doi.org/10.1038/s41598-018-26551-w.

[62] S. Han, J. Sun, S. He, M. Tang, R. Chai, The application of graphene-based biomaterials in biomedicine, Am. J. Transl. Res. 11 (2019) 3246-3260.

[63] J.K. Park, J. Jung, P. Subramaniam, B.P. Shah, C. Kim, J.K. Lee, J.H. Cho, C. Lee, K.B. Lee, Graphite- Coated Magnetic Nanoparticles as Multimodal Imaging Probes and Cooperative Therapeutic Agents for Tumor Cells, Small. 7 (2011) 1647-1652. https://doi.org/10.1002/smll.201100012.

[64] H. Sun, L. Wu, N. Gao, J. Ren, X. Qu, Improvement of photoluminescence of graphene quantum dots with a biocompatible photochemical reduction pathway and its bioimaging application, ACS Appl. Mater Interfaces. 5 (2013) 1174-1179. https://doi.org/10.1021/am3030849.

[65] K. Yang, L. Feng, X. Shi, Z. Liu, Nano-graphene in biomedicine: theranostic applications, Chem. Soc. Rev. 42 (2013) 530-547. https://doi.org/10.1039/C2CS35342C.

[66] C. Chung, Y.-K. Kim, D. Shin, S.-R. Ryoo, B.H. Hong, D.-H. Min, Biomedical applications of graphene and graphene oxide, Acc. Chem. Res. 46 (2013) 2211-2224. https://doi.org/10.1021/ar300159f.

[67] M. Gu, Y. Liu, T. Chen, F. Du, X. Zhao, C. Xiong, Y. Zhou, Is graphene a promising nano-material for promoting surface modification of implants or scaffold materials in bone tissue engineering?, Tissue Eng. Part B Rev. 20 (2014) 477-491. https://doi.org/10.1089/ten.teb.2013.0638.

[68] W.C. Lee, C.H.Y.X. Lim, H. Shi, L.A.L. Tang, Y. Wang, C.T. Lim, K.P. Loh, Origin of enhanced stem cell growth and differentiation on graphene and graphene oxide, ACS nano. 5 (2011) 7334-7341. https://doi.org/10.1021/nn202190c.

[69] M. Nair, D. Nancy, A.G. Krishnan, G.S. Anjusree, S. Vadukumpully, S.V. Nair, Graphene oxide nanoflakes incorporated gelatin–hydroxyapatite scaffolds enhance osteogenic differentiation of human mesenchymal stem cells, Nanotechnol. 26 (2015) 161001. https://doi.org/10.1088/0957-4484/26/16/161001.

[70] G.Y. Chen, D.-P. Pang, S.M. Hwang, H.Y. Tuan, Y.C. Hu, A graphene-based platform for induced pluripotent stem cells culture and differentiation, Biomater. 33 (2012) 418-427. https://doi.org/10.1016/j.biomaterials.2011.09.071.

[71] X. Xiaozhi, Z. Zhihong, D. Jichen, Y. Ding, N. Jingjing, W. Muhong, L. Li, Y. Rongkang, L. Mingqiang, Z. Jingyuan, Ultrafast epitaxial growth of metre-sized single-crystal graphene on industrial Cu foil, Sci. Bull. 62 (2017) 1074-1080. https://doi.org/10.1016/j.scib.2017.07.005.

[72] K. Li, C. Wang, J. Yan, Q. Zhang, B. Dang, Z. Wang, Y. Yao, K. Lin, Z. Guo, L. Bi, Evaluation of the osteogenesis and osseointegration of titanium alloys coated with graphene: an in vivo study, Sci. Rep. 8 (2018) 1843. https://doi.org/10.1038/s41598-018-19742-y.

[73] Y. Li, C. Yang, H. Zhao, S. Qu, X. Li, Y. Li, New developments of Ti-based alloys for biomedical applications, Materials. 7 (2014) 1709-1800. https://doi.org/10.3390/ma7031709.

[74] G. Lütjering, J.C. Williams, Titanium, Second ed., Springer Science & Business Media, Heildelberg, Germany, 2007.

[75] in: ASTM E9-89a. Standard Test Methods of Compression Testing of Metallic Materials at Room Temperature, ASTM International, West Conshohocken, PA,, 2000.

[76] in: ISO 13314: 2011 (E) Mechanical testing of metals—ductility testing—compression test for porous and cellular metals, 2011, pp. 1-7.

[77] Y. Li, J. Xiong, C.S. Wong, P.D. Hodgson, C.e. Wen, Ti6Ta4Sn alloy and subsequent scaffolding for bone tissue engineering, Tissue Eng. Part A. 15 (2009) 3151-3159. https://doi.org/10.1016/S1003-6326(12)61705-1.

[78] in: ASTM C373-18-Standard Test Methods for Determination of Water Absorption and Associated Properties by Vacuum Method for Pressed Ceramic Tiles and Glass Tiles and Boil Method for Extruded Ceramic Tiles and Non-tile Fired Ceramic Whiteware Products, ASTM International West Conshohocken, PA, 2018.

[79] R.M. Christensen, Observations on the Definition of Yield Stress, Acta Mech. 196 (2008) 239-244. https://doi.org/10.1007/s00707-007-0478-0.

[80] L.F. Nielsen, Elasticity and Damping of Porous Materials and Impregnated Materials, J Am Cer Soc. 67 (1984) 93-98. https://doi.org/10.1111/j.1151-2916.1984.tb09622.x.

[81] A.M. Khorasani, M. Goldberg, E.H. Doeven, G. Littlefair, Titanium in biomedical applications—properties and fabrication: a review, J. Biomater. Tissue. Eng. 5 (2015) 593-619. https://doi.org/10.1166/jbt.2015.1361.

[82] E. Zurob, G. Dennett, D. Gentil, F. Montero-Silva, U. Gerber, P. Naulín, A. Gómez, R. Fuentes, S. Lascano, T.H. Rodrigues da Cunha, Inhibition of Wild Enterobacter cloacae Biofilm Formation by Nanostructured Graphene-and Hexagonal Boron Nitride-Coated Surfaces, Nanomater. 9 (2019) 49. https://doi.org/10.3390/nano9010049.

[83] C. Parra, F. Montero-Silva, D. Gentil, V. Del Campo, T. Henrique Rodrigues da Cunha, R. Henríquez, P. Häberle, C. Garín, C. Ramírez, R. Fuentes, The many faces of graphene as protection barrier. performance under microbial corrosion and Ni allergy conditions, Materials. 10 (2017) 1406. https://doi.org/10.3390/ma10121406.

[84] C. Parra, F. Dorta, E. Jimenez, R. Henríquez, C. Ramírez, R. Rojas, P. Villalobos, A nanomolecular approach to decrease adhesion of biofouling-producing bacteria to graphene-coated material, J. Nanobiotechnol. 13 (2015) 82. https://doi.org/10.1186/s12951-015-0137-x.

[85] B. Thiel, Variable Pressure Scanning Electron Microscopy, in: Springer Handbook of Microscopy, Springer, 2019, pp. 2-2.

[86] C.A. Acevedo, Y. Olguín, M. Briceño, J.C. Forero, N. Osses, P. Díaz-Calderón, A. Jaques, R. Ortiz, Design of a biodegradable UV-irradiated gelatin-chitosan/nanocomposed membrane with osteogenic ability for application in bone regeneration, Mater. Sci. Eng., C. 99 (2019) 875-886. https://doi.org/10.1016/j.msec.2019.01.135.

[87] in: ISO 10993–5: 2009 Biological Evaluation of Medical Devices—Part 5: Tests for In Vitro Cytotoxicity, Geneva, Switzerland, 2009.

[88] Y.-q. Wang, J. Tao, J.-l. Zhang, T. Wang, Effects of addition of NH4HCO3 on pore characteristics and compressive properties of porous Ti-10%Mg composites, T Nonferr Met Soc. 21 (2011) 1074-1079. https://doi.org/10.1016/S1003-6326(11)60824-8.

[89] J. Rivard, V. Brailovski, S. Dubinskiy, S. Prokoshkin, Fabrication, morphology and mechanical properties of Ti and metastable Ti-based alloy foams for biomedical applications, Mater. Sci. Eng., C. 45 (2014) 421-433. https://doi.org/10.1016/j.msec.2014.09.033.

[90] C. Xiang, Y. Zhang, Z. Li, H. Zhang, Y. Huang, H. Tang, 2011 Chinese Materials ConferencePreparation and compressive behavior of porous titanium prepared by space holder sintering process, Procedia Engineer. 27 (2012) 768-774. https://doi.org/10.1016/j.proeng.2011.12.518.

[91] X. Liu, M.N. Rahaman, Q. Fu, Bone regeneration in strong porous bioactive glass (13-93) scaffolds with an oriented microstructure implanted in rat calvarial defects, Acta Biomater. 9 (2013) 4889-4898. https://doi.org/10.1016/j.actbio.2012.08.029.

[92] X. Rao, C.L. Chu, Y.Y. Zheng, Phase composition, microstructure, and mechanical properties of porous Ti–Nb–Zr alloys prepared by a two-step foaming powder metallurgy method, J Mech Behav Biomed Mater. 34 (2014) 27-36. https://doi.org/10.1016/j.jmbbm.2014.02.001.

[93] A.G. Mitsak, J.M. Kemppainen, M.T. Harris, S.J. Hollister, Effect of polycaprolactone scaffold permeability on bone regeneration in vivo, Tissue Eng. Part A. 17 (2011) 1831-1839. https://doi.org/10.1089/ten.tea.2010.0560.

[94] T.N. Vo, F.K. Kasper, A.G. Mikos, Strategies for controlled delivery of growth factors and cells for bone regeneration, Adv Drug Deliver Rev. 64 (2012) 1292-1309. https://doi.org/10.1016/j.addr.2012.01.016.

[95] S. Muñoz, J. Pavón, J.A. Rodríguez-Ortiz, A. Civantos, J.P. Allain, Y. Torres, On the influence of space holder in the development of porous titanium implants: Mechanical, computational and biological evaluation, Mater Charact. 108 (2015) 68-78. https://doi.org/10.1016/j.matchar.2015.08.019.

[96] J. Jia, A.R. Siddiq, A.R. Kennedy, Porous titanium manufactured by a novel powder tapping method using spherical salt bead space holders: Characterisation and mechanical properties, J Mech Behav Biomed Mater. . 48 (2015) 229-240. https://doi.org/10.1016/j.jmbbm.2015.04.018.

[97] K.S. Dragolich, N.D. DiMatteo, Fatigue data book: light structural alloys, ASM International, 1994.

[98] H. Baker, H. Okamoto, Alloy phase diagrams, in: ASM International, ASM Handbook., 1992, pp. 501.

[99] F.H. Cocks, R.M. Rose, J. Wulff, Niobium-Tantalum-Titanium Ternary Alloy Phase Diagram, in: ASM Alloy Phase Diagrams Center, ASM, 2007.

[100] A.L. Gavzeo, P.B. Budberg, S.A. Minayeva, Niobium-Tantalum-Titanium Ternary Alloy Phase Diagram, in: Handbook ASM Alloy Phase Diagrams, ASM, 2007.

[101] R.L. Morrison, in, US5382285A, 1995.

[102] H.K. Kleinman, K.M. Malinda, A.L. Goldstein, G. Sosne, in, US20070015698A1, 2012.

[103] R.B. Kaplan, in, US5282861A, 1994.

[104] J.E. Hall, A.C. Guyton, in: J.E. Hall (Ed.), Elsevier, 2016.

[105] G. Lewis, Properties of open-cell porous metals and alloys for orthopaedic applications, J Mater Sci-Mater M. 24 (2013) 2293-2325. https://doi.org/10.1007/s10856-013-4998-y.

[106] R. Singh, P.D. Lee, J.R. Jones, G. Poologasundarampillaia, T. Post, T.C. Lindley, R.J. Dashwood, Hierarchically structured titanium foams for tissue scaffold applications, Acta Biomater. 6 (2010) 4596-4604. https://doi.org/10.1016/j.actbio.2010.06.027.

[107] S.C.P. Cachinho, R.N. Correia, Titanium scaffolds for osteointegration: mechanical, in vitro and corrosion behaviour, J Mater Sci-Mater M. 19 (2008) 451-457. https://doi.org/10.1007/s10856-006-0052-7.

[108] G. Mendonça, D.B. Mendonça, F.J. Aragao, L.F. Cooper, Advancing dental implant surface technology–from micron-to nanotopography, Biomater. 29 (2008) 3822-3835. https://doi.org/10.1016/j.biomaterials.2008.05.012.

[109] D. Khang, J. Lu, C. Yao, K.M. Haberstroh, T.J. Webster, The role of nanometer and sub-micron surface features on vascular and bone cell adhesion on titanium, Biomater. 29 (2008) 970-983. https://doi.org/10.1016/j.biomaterials.2007.11.009.

[110] N. Dubey, J.L.P. Morin, E.K. Luong-Van, S.V. Agarwalla, N. Silikas, A.C. Neto, V. Rosa, Osteogenic potential of graphene coated titanium is independent of transfer technique, Materialia. 9 (2020) 100604. https://doi.org/10.1016/j.mtla.2020.100604.

[111] R. Malhotra, Y. Han, J. Morin, E. Luong-Van, R. Chew, A. Castro Neto, C. Nijhuis, V. Rosa, Inhibiting Corrosion of Biomedical-Grade Ti-6Al-4V Alloys with Graphene Nanocoating, J. Dent. Res. 99 (2020) 285-292. https://doi.org/10.1177/0022034519897003.

[112] S. Das, D. Lahiri, D.-Y. Lee, A. Agarwal, W. Choi, Measurements of the adhesion energy of graphene to metallic substrates, Carbon. 59 (2013) 121-129. https://doi.org/10.1016/j.carbon.2013.02.063.

[113] G. Schmidmaier, B. Wildemann, P. Schwabe, R. Stange, J. Hoffmann, N. Südkamp, N. Haas, M. Raschke, A new electrochemically graded hydroxyapatite coating for osteosynthetic implants promotes implant osteointegration in a rat model, J Biomed Mater Res B. 63 (2002) 168-172. https://doi.org/10.1002/jbm.10130.

[114] C. Parra, F. Montero-Silva, R. Henríquez, M. Flores, C. Garín, C. Ramírez, M. Moreno, J. Correa, M. Seeger, P. Häberle, Suppressing bacterial interaction with copper surfaces through graphene and hexagonal-boron nitride coatings, ACS Appl. Mater Interfaces. 7 (2015) 6430-6437. https://doi.org/10.1021/acsami.5b01248.

[115] W. Jin, Q. Hao, X. Peng, P.K. Chu, Enhanced corrosion resistance and biocompatibilty of PMMA-coated ZK60 magnesium alloy, Mater. Lett. 173 (2016) 178-181. https://doi.org/10.1016/j.matlet.2016.03.071.

[116] J.W. Suk, A. Kitt, C.W. Magnuson, Y. Hao, S. Ahmed, J. An, A.K. Swan, B.B. Goldberg, R.S. Ruoff, Transfer of CVD-grown monolayer graphene onto arbitrary substrates, ACS nano. 5 (2011) 6916-6924. https://doi.org/10.1021/nn201207c.

[117] W. Zhou, Z. Han, J. Wang, Y. Zhang, Z. Jin, X. Sun, Y. Zhang, C. Yan, Y. Li, Copper catalyzing growth of single-walled carbon nanotubes on substrates, Nano lett. 6 (2006) 2987-2990. https://doi.org/10.1021/nl061871v.

[118] R. Gautam, R.D. Singh, V.P. Sharma, R. Siddhartha, P. Chand, R. Kumar, Biocompatibility of polymethylmethacrylate resins used in dentistry, J Biomed Mater Res B. 100 (2012) 1444-1450. https://doi.org/10.1002/jbm.b.32673.

[119] S. Kasap, H. Khaksaran, S. Çelik, H. Özkaya, C. Yanık, I.I. Kaya, Controlled growth of large area multilayer graphene on copper by chemical vapour deposition, Phys. Chem. Chem. Phys. 17 (2015) 23081-23087. https://doi.org/10.1039/C5CP01436K.

[120] Y. Shimakawa, Y. Kubo, Y. Tauchi, T. Kamiyama, H. Asano, F. Izumi, Structural distortion and ferroelectric properties of SrBi 2 (Ta 1− x Nb x) 2 O 9, Appl Phys Lett. 77 (2000) 2749-2751. https://doi.org/10.1063/1.1319509.

[121] M.R. Islam, R.H. Galib, A. Sharif, M. Hasan, M.A. Zubair, M.F. Islam, Correlation of charge defects and morphology with magnetic and electrical properties of Sr and Ta codoped BiFeO3, J. Alloy Compd. 688 (2016) 1186-1194. https://doi.org/10.1016/j.jallcom.2016.07.134.

[122] D. Sharma, R. Jha, Transition metal (Co, Mn) co-doped ZnO nanoparticles: effect on structural and optical properties, J. Alloy Compd. 698 (2017) 532-538. https://doi.org/10.1016/j.jallcom.2016.12.227.

[123] R. Rodriguez y Baena, S. Rizzo, L. Manzo, S.M. Lupi, Nanofeatured titanium surfaces for dental implantology: biological effects, biocompatibility, and safety, Journal of Nanomaterials. 2017 (2017) 18. https://doi.org/10.1155/2017/6092895.

Figure 1. Diagram representing the PMMA-assisted transfer method used to obtain graphene-coated Ti-35Nb-29Ta-4Mn foam samples.

Figure 2. Optical micrographs of foams obtained by space-holder technique: (a) c.p. Ti–Tsint: 1250 °C; (b) 4 wt.% Mn– Tsint: 1200 °C; (c) 4 wt.% Mn – Tsint: 1300 °C. SEM micrographs showing wall thickness (d) 1200 ºC and (e) 1300 °C and inner porous roughness (f) 1200 °C and (g) 1300 ºC.

Figure 3. Pore size distribution: (a) 1200 °C and b) 1300 °C.

Figure 4. XRD patterns of samples Ti-35Nb-29Ta-xMn sintered at: (a) 1200 °C and (b) 1300 °C. The Ti-β phase, Nb and Ta have the same crystalline structure and space group (Im-3m), with XRD peaks very close in 2θ values. Indexing was performed using the following reference diffraction patterns from the PDF-4+ database of the International Centre for Diffraction Data (ICDD): Ti-β (44-1288), Ti-α (44-1294), Nb (34-0370), Ta (04-0788) and Mn (32-0637).

Figure 5. TEM characterization of foams with 4 wt.% Mn at 1200 ºC: (a) TEM image and polycrystalline electron diffraction pattern; (b) HR-TEM image and specific areas Fast Fourier Transformation.

Figure 6. Mechanical behavior of Ti-35Nb-29Ta-xMn (x: 2, 4, 6 wt.%) foams: (a) 1200 °C; (b) 1300 °C. Effect of temperature and wt.% Mn on ductility and strength in porous structures of titanium alloys produced via space-holder.

Figure 7. (a) Large-scale STM topography (120 × 120 nm^2) of single-layer graphene grown on Cu; (b) High-magnification STM image (1.3 × 1.3 nm^2) showing the hexagonal lattice atomic structure of single-layer graphene on Cu with lattice constant 2.4 Å, according to Fourier transform analysis (inset). Tunnel current and bias voltages were between 0.1 and 0.9 nA and

0.05–1 V; (c) Raman spectra of transferred graphene over SiO_2; (d) Raman spectra of monolayer graphene on substrates: on a solid surface of the foam (blue), and suspended on a pore (red). MO images of areas where Raman spectra of (e) graphene on porous substrate and (f) graphene suspended on pore were obtained.

Figure 8. Optical micrograph of 4 wt.% Mn: (a) substrates coated with a SLG; (b) Detail of PMMA residues on SLG coatings at high magnification (dark field); SEM micrographs of substrates coated with SLG on solid surface, showing (c) wrinkles on SLG coating, and (d) graphene suspended on pores and roughness inside of pores.

Figure 9. Growth of MEF cells with liquid extract and direct contact onto graphene-coated material.

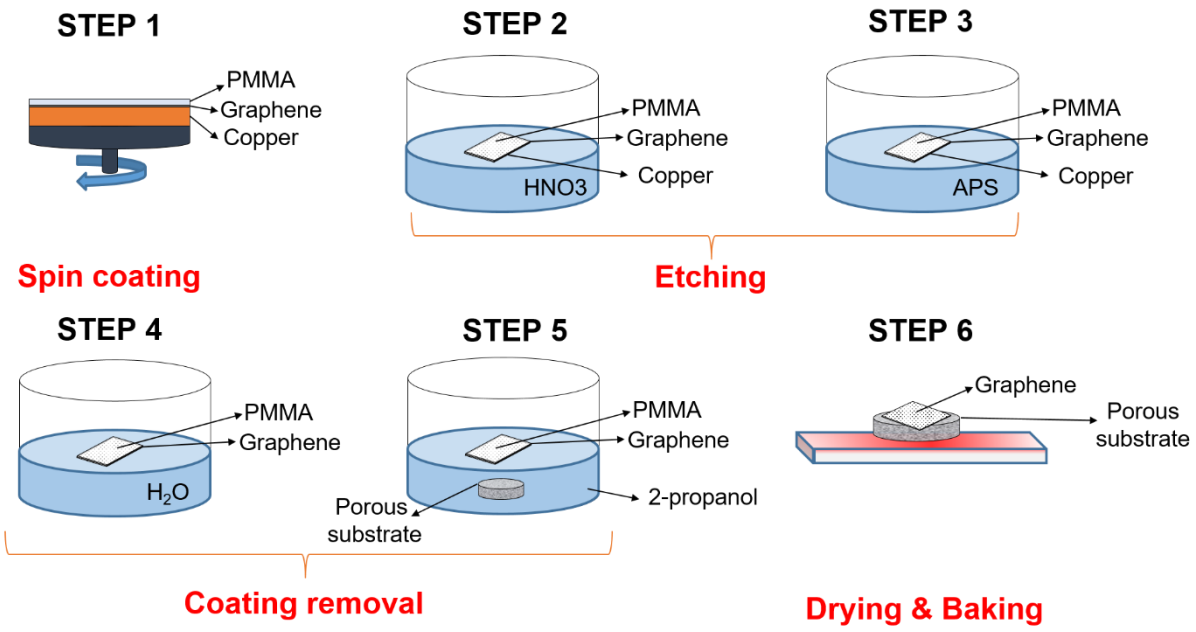
STEP 1
PMMA
Graphene
Copper
STEP 2
PMMA
Graphene
HNO3
Copper
STEP 3
PMMA
Graphene
APS
Copper
Spin coating
Etching
STEP 4
PMMA
Graphene
H2O
STEP 5
PMMA
Graphene
Porous substrate
2-propanol
STEP 6
Graphene
Porous substrate
Coating removal
Drying & Baking

1

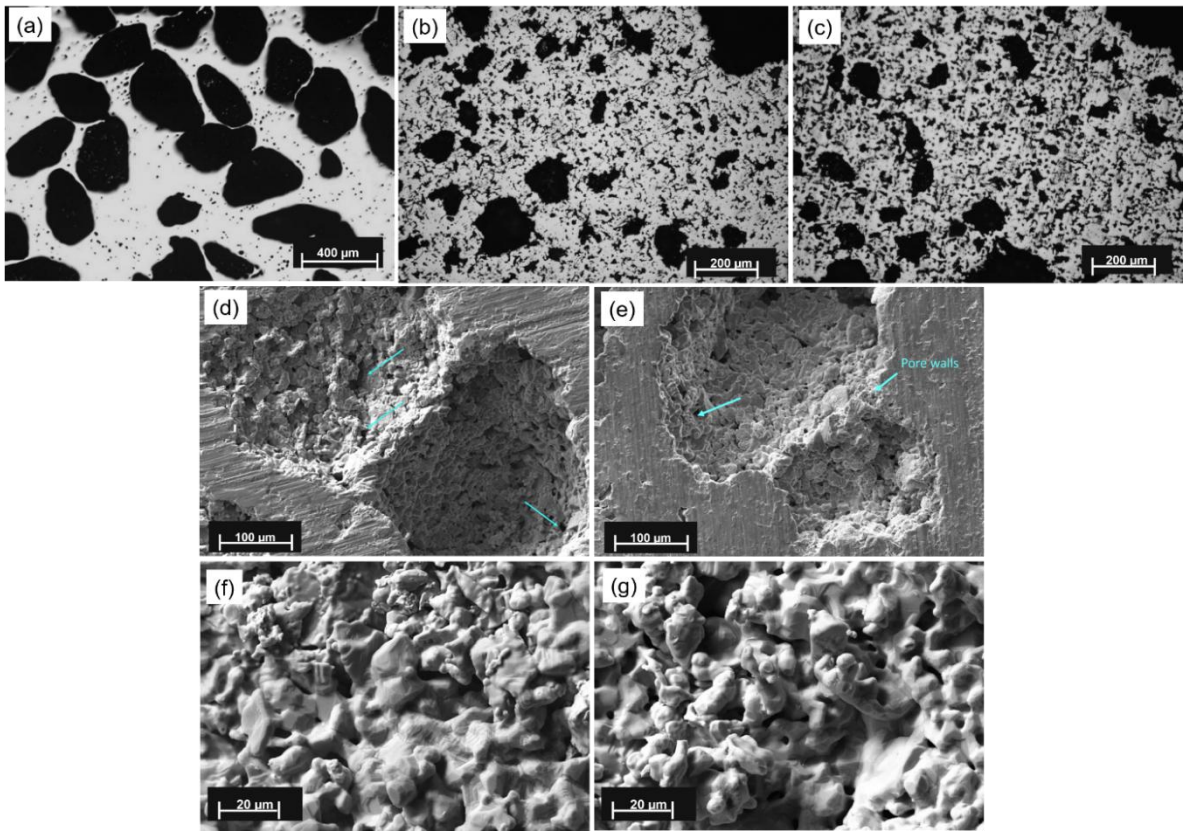

2

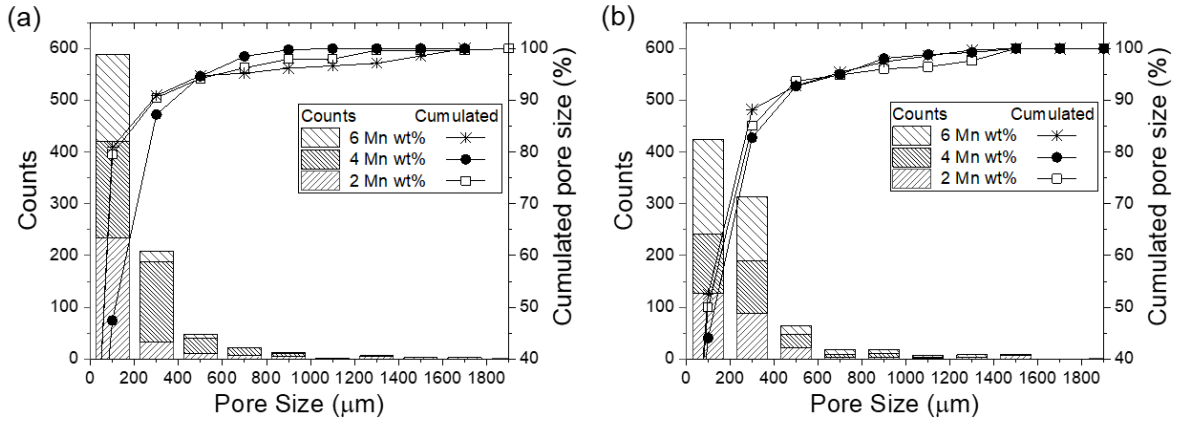
(a)
(b)
Counts
Cumulated pore size (%)
Pore Size (μm)
Counts
Cumulated
6 Mn wt%
4 Mn wt%
2 Mn wt%

3

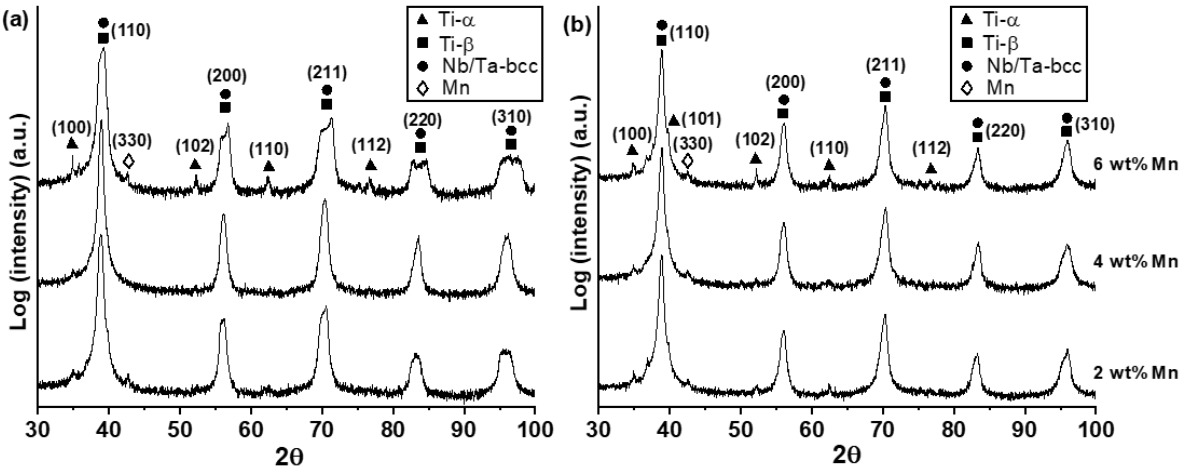
(a)
(b)
Ti-α
Ti-β
Nb/Ta-bcc
Mn
(100)
(101)
(110)
(200)
(211)
(102)
(330)
(112)
(220)
(310)
Log (intensity) (a.u.)
2θ
6 wt% Mn
4 wt% Mn
2 wt% Mn

4

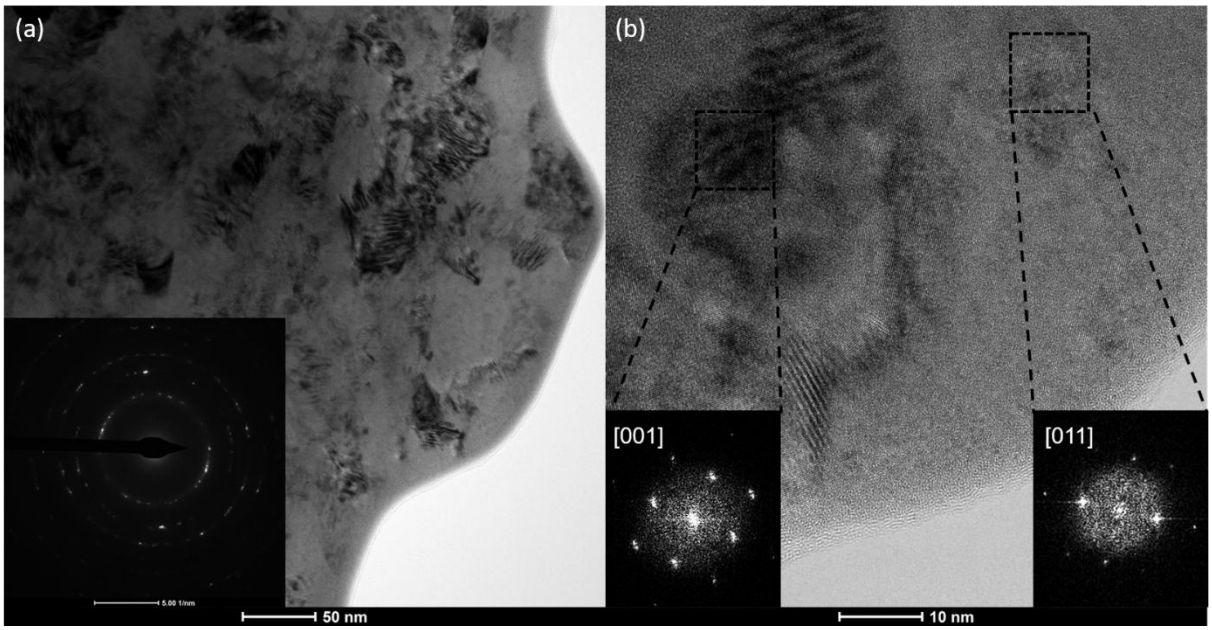

5

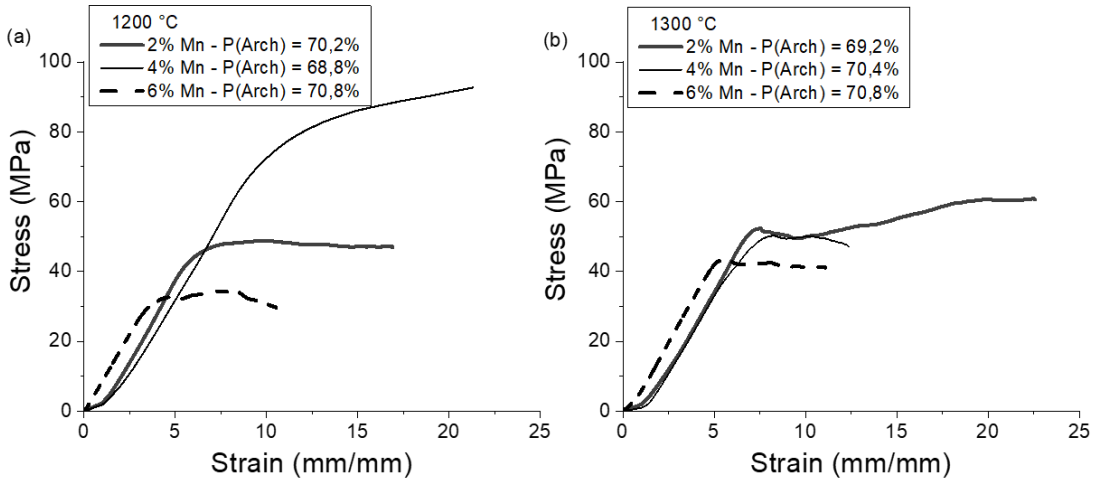
(a)
1200 °C
2% Mn - P(Arch) = 70,2%
4% Mn - P(Arch) = 68,8%
6% Mn - P(Arch) = 70,8%
Stress (MPa)
Strain (mm/mm)
(b)
1300 °C
2% Mn - P(Arch) = 69,2%
4% Mn - P(Arch) = 70,4%
6% Mn - P(Arch) = 70,8%
Stress (MPa)
Strain (mm/mm)

6

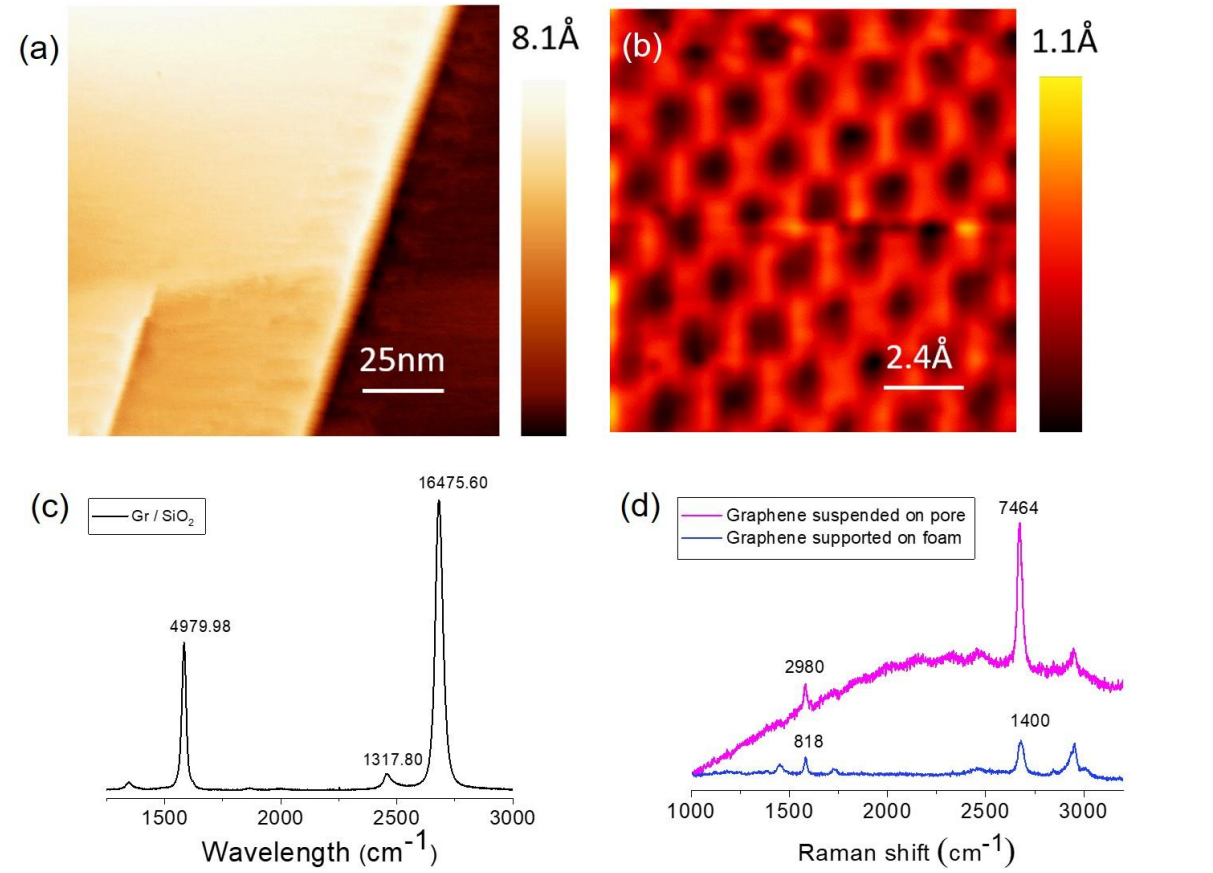
(a)
8.1Å
25nm
(b)
1.1Å
2.4Å
(c)
Gr / SiO2
16475.60
4979.98
1317.80
1500
2000
2500
3000
Wavelength (cm-1)
(d)
Graphene suspended on pore
Graphene supported on foam
7464
2980
1400
818
1000
1500
2000
2500
3000
Raman shift (cm-1)
(e)
10 µm
10 µm
(f)
10 µm
10 µm

7

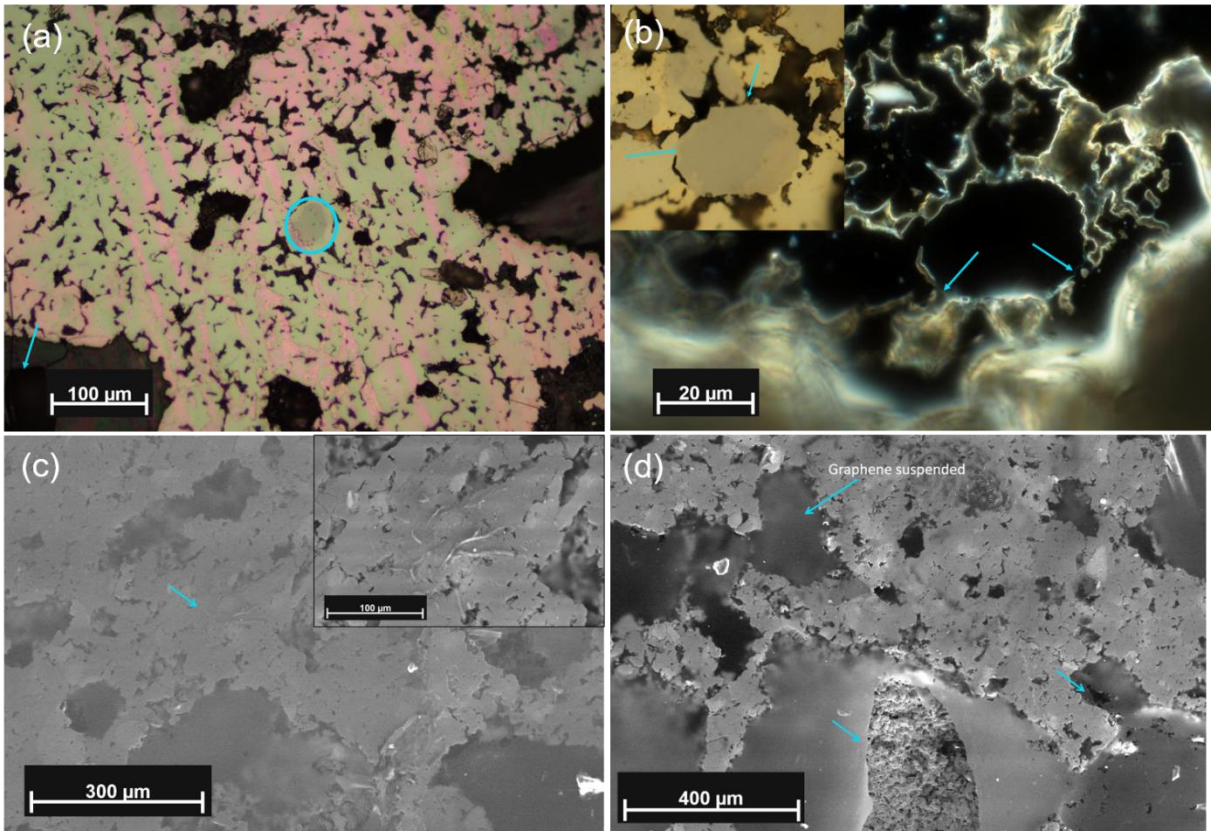

8

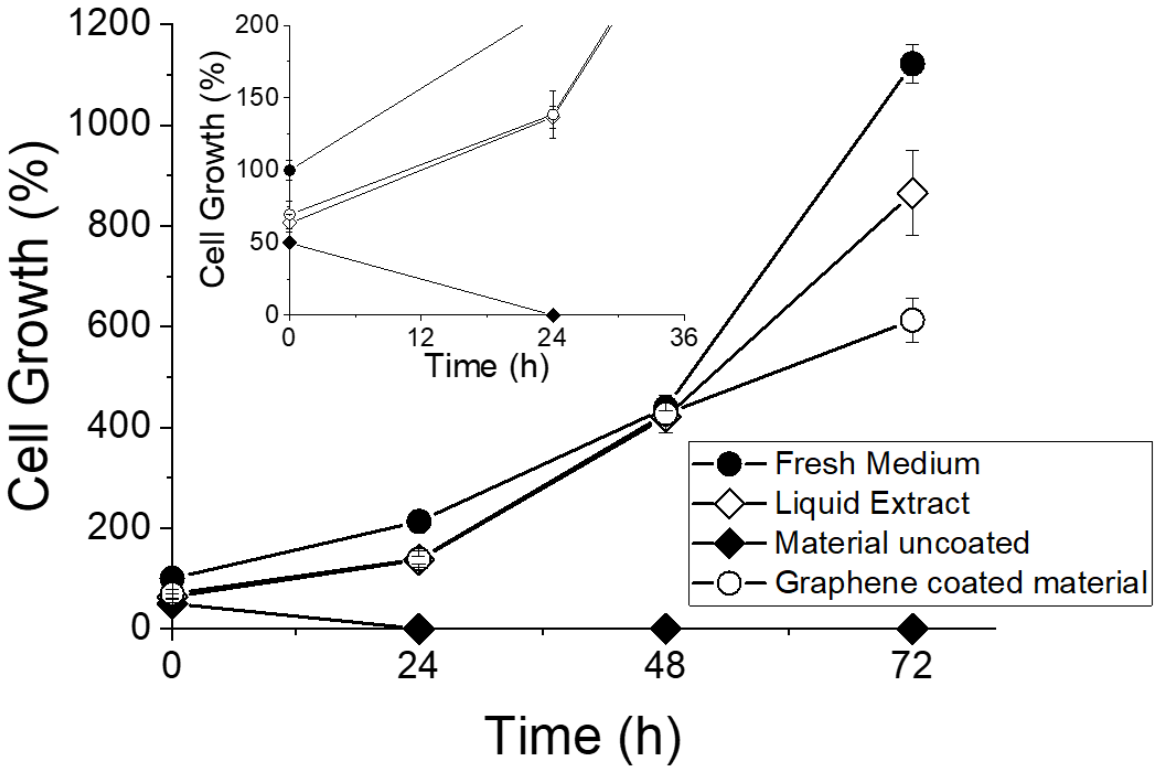
Cell Growth (%)
Time (h)
Fresh Medium
Liquid Extract
Material uncoated
Graphene coated material
0
200
400
600
800
1000
1200
0
24
48
72
Cell Growth (%)
Time (h)
0
50
100
150
200
0
12
24
36

9

Supplementary Material

Click here to download Supplementary Material: Supporting Information (reviewed).docx

CRediT author statement

The manuscript was written with the contributions of all authors. All authors have given approval to the final version of the manuscript. **Sheila Lascano**: Investigation, Writing- Review & Editing, Funding acquisition, **Ricardo Chávez-Vásconez**: Investigation, Formal analysis, Writing, **Daniela Muñoz-Rojas**: Investigation, Formal analysis, **Juliet Aristizabal**: Investigation, Writing- Original Draft, **Bárbara Arce**: Investigation, **Carolina Parra**: Investigation, Resources, Writing- Review & Editing, **Cristian Acevedo**: Investigation, Resources and Writing, **Nicole Orellana**: Investigation, Formal Analysis, **Mauricio Reyes-Valenzuela**: Investigation, Formal Analysis, **Francisco José Gotor**: Formal Analysis, Review & Editing, **Cristina Arévalo**: Investigation, Resources, Writing- Review & Editing, **Yadir Torres**: Investigation, Review & Funding acquisition